Article

Neuron

Development and Refinement of Functional Properties of Adult-Born Neurons

Highlights

- Adult-born granule cells (abGCs) respond to odors soon after arrival in the bulb
- Most abGCs become more narrowly tuned to odors in the first 3 weeks of development
- A subpopulation of abGCs becomes more broadly tuned during their maturation
- Olfactory enrichment prolongs the period over which abGCs are strongly responsive

Authors

Jenelle L. Wallace, Martin Wienisch, Venkatesh N. Murthy

Correspondence

wienisch@mit.edu (M.W.), vnmurthy@fas.harvard.edu (V.N.M.)

In Brief

Using multiphoton imaging in awake and anesthetized mice, Wallace, Wienisch, et al. track the functional maturation of individual adult-born granule cells of the olfactory bulb, showing that most cells become more selective in their odor responses during maturation.

Wallace et al., 2017, Neuron *96*, 1–14
November 15, 2017 © 2017 Elsevier Inc.
https://doi.org/10.1016/j.neuron.2017.09.039

CellPress

Please cite this article in press as: Wallace et al., Development and Refinement of Functional Properties of Adult-Born Neurons, Neuron (2017), https://doi.org/10.1016/j.neuron.2017.09.039

Neuron
Article

CellPress

Development and Refinement of Functional Properties of Adult-Born Neurons

Jenelle L. Wallace,[1,2,3,5] Martin Wienisch,[2,3,4,5,*] and Venkatesh N. Murthy[2,3,6,*]
[1]Molecules, Cells, and Organisms training program
[2]Center for Brain Science
[3]Department of Molecular & Cellular Biology
Harvard University, Cambridge, MA 02138, USA
[4]Present address: McGovern Institute for Brain Research, Department of Brain and Cognitive Sciences, Massachusetts Institute of Technology, Cambridge, MA 02139, USA
[5]These authors contributed equally
[6]Lead Contact
*Correspondence: wienisch@mit.edu (M.W.), vnmurthy@fas.harvard.edu (V.N.M.)
https://doi.org/10.1016/j.neuron.2017.09.039

SUMMARY

New neurons appear only in a few regions of the adult mammalian brain and become integrated into existing circuits. Little is known about the functional development of individual neurons *in vivo*. We examined the functional life history of adult-born granule cells (abGCs) in the olfactory bulb using multiphoton imaging in awake and anesthetized mice. We found that abGCs can become responsive to odorants soon after they arrive in the olfactory bulb. Tracking identified abGCs over weeks revealed that the robust and broadly tuned responses of most newly arrived abGCs gradually become more selective over a period of ~3 weeks, but a small fraction achieves broader tuning with maturation. Enriching the olfactory environment of mice prolonged the period over which abGCs were strongly and broadly responsive to odorants. Our data offer direct support for rapid integration of adult-born neurons into existing circuits, followed by experience-dependent refinement of their functional connectivity.

INTRODUCTION

The addition of new neurons to the adult brain represents a dramatic form of plasticity present in only a few areas of the rodent brain, including the olfactory bulb (OB) and the dentate gyrus (DG). A surge of studies in the past decade has begun to investigate the mechanisms and implications of ongoing cell turnover in these brain areas (Kempermann et al., 2015; Lepousez et al., 2013; Lledo et al., 2006; Sahay et al., 2011), yet it is still unclear how adult-born neurons functionally integrate into an intact circuit. The OB provides an excellent system for investigating this process because of the direct relationship between olfactory stimuli and neural responses.

Adult neurogenesis is thought to enhance plasticity in OB circuits and could optimize olfactory processing for certain types of olfactory behaviors (Alonso et al., 2012; Chow et al., 2012; Malvaut and Saghatelyan, 2016; Mandairon et al., 2011; Moreno et al., 2009; Mouret et al., 2009; Sakamoto et al., 2011). Adult-born granule cells (abGCs) in the OB are the most abundant type of adult-born neuron in the mouse brain, yet it is unknown when they first become responsive to olfactory stimuli and how these responses change as they mature.

AbGCs migrate along the rostral migratory stream (RMS) and arrive in the OB beginning about 7 days after their birth in the subventricular zone (SVZ) (Lois and Alvarez-Buylla, 1994; Yamaguchi and Mori, 2005). They rapidly develop dendritic trees (Lledo et al., 2006; Petreanu and Alvarez-Buylla, 2002), and over the next few weeks, they receive inputs from local inhibitory interneurons (Pallotto et al., 2012; Panzanelli et al., 2009) and later increasing numbers of excitatory inputs (Carleton et al., 2003; Kelsch et al., 2008; Ravi et al., 2017; Whitman and Greer, 2007) from olfactory cortex and neuromodulatory inputs (Moreno et al., 2012; Veyrac et al., 2009), as well as excitatory synapses from M/T cells, which are also the major target of GC outputs (Urban and Arevian, 2009). During synaptogenesis, there is a critical period in which abGCs are particularly sensitive to environmental influences, including olfactory experience or deprivation, which can affect synapse number and cell survival (Kelsch et al., 2009; Lin et al., 2010; Saghatelyan et al., 2005; Winner et al., 2002; Yamaguchi and Mori, 2005). Despite this work, it is still unclear how abGCs respond to stimuli *in vivo*, which is difficult to predict from the number of synaptic inputs alone.

Several studies have begun to address the *in vivo* responses of adult-born neurons using a variety of approaches. A pioneering study using the immediate early gene (IEG) cfos found that abGCs were more responsive than pre-existing GCs to novel odors 2–3 weeks after their generation and then became less responsive over time (Magavi et al., 2005). Two other recent studies examined *in vivo* response properties of different

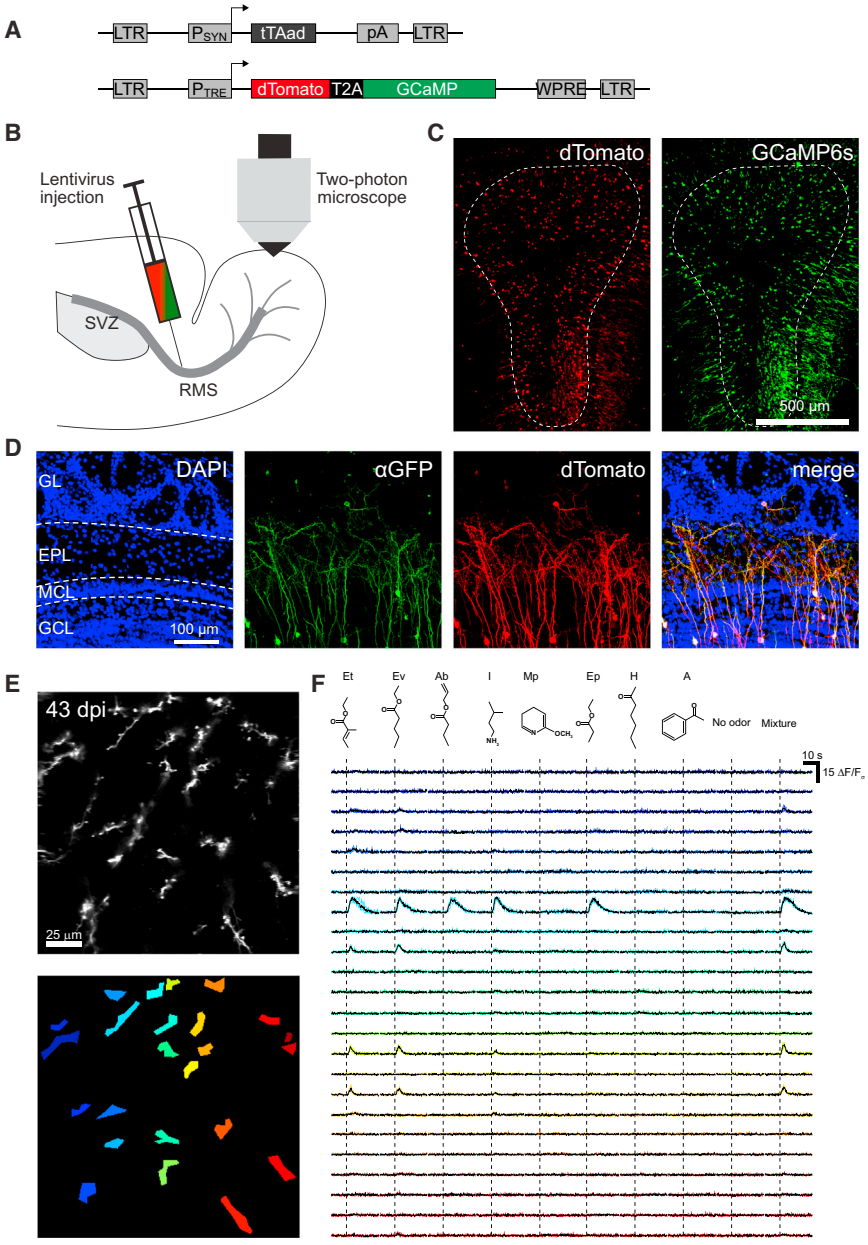

Figure 1. Optical Recordings of Odor-Evoked Activity in abGCs

(A) Constructs used in the study. Tetracycline transactivator protein (tTAd) is expressed under control of the synapsin promoter (above), which activates the tetracycline response element (TRE) promoter and controls the expression of dTomato and GCaMP5 or GCaMP6s (below).

(B) Lentivirus was injected into the RMS and imaging of the olfactory bulb was performed with a two-photon microscope.

(C) Coronal view of the olfactory bulb showing lentiviral-expressed dTomato and GCaMP6s and the distribution of labeled abGCs. Dotted line shows the superficial boundary of the GCL.

(D) Immunostaining confirms dual expression of reporters in abGCs.

(E) Top: average intensity projection showing an example imaging field (dTomato channel) with abGC dendrites in the EPL *in vivo* at 43 dpi. Bottom: in each imaging field, individual dendrites were outlined manually and a mask of these ROIs was used to calculate fluorescence changes.

(F) Traces ($\Delta F/F_{\sigma}$, GCaMP6s) for all dendrites labeled in (E) are shown (colors) along with the average trace (black) for four repetitions of all odorants in set B.

GL, glomerular layer; EPL, external plexiform layer; MCL, mitral cell layer; GCL, granule cell layer.

classes of adult-born neurons (periglomerular neurons in the bulb [Livneh et al., 2014] and granule cells in the DG [Danielson et al., 2016]) using targeted patch-clamp recordings and GCaMP imaging, respectively. These studies also showed that immature adult-born neurons tended to be more responsive and broadly tuned than mature cells. However, a more recent study using epifluorescence and multiphoton calcium imaging suggested that abGC maturation may instead follow an opposite trend, with broader tuning curves observed in putative mature cells (older than 4 weeks, labeled in the Crhr1 Cre line) than in younger cells (between 3 and 4 weeks old, labeled in the Dlx5/6 Cre line) (Quast et al., 2017). Despite the advantages of such genetic strategies for widespread labeling, it is still unclear whether they target cell populations equivalent to those labeled by the extensively validated, nucleotide-based (Gratzner, 1982; Yamaguchi and Mori, 2005) or lentiviral (Kopel et al., 2009; Lepousez et al., 2014) labeling methods. In addition, genetic methods necessarily rely on studying populations of neurons at different time points, which precludes the characterization of the developmental process in individual adult-born cells and is likely to be particularly important in light of the extensive heterogeneity reported among granule cells (Naritsuka et al., 2009; Orona et al., 1983). In this study, we chose to use two-photon imaging of identified abGCs over time to characterize, for the first time, how the odorant responses of individual abGCs change as they integrate into the olfactory circuit, beginning at the earliest stages yet examined *in vivo*.

RESULTS

Imaging Activity in abGCs

We labeled adult-born neurons sparsely using lentiviral injection into the RMS. We used the Tet-Off system (Hioki et al., 2009) to produce specific, fast, and high expression levels of reporters when activated by tTAad (in the absence of doxycycline), which in turn is driven by the neuron-specific synapsin promoter (Figures 1A and 1B). Our lentiviral construct contained both a morphological marker (dTomato) and a calcium indicator (GCaMP5 or

GCaMP6s). We confirmed dual expression of dTomato and GCaMP in abGCs (Figures 1C and 1D; Figure S1). We implanted mice with chronic cranial windows and used multiphoton microscopy to image dendrites of abGCs. Adult-born granule cell bodies were located in the mitral cell layer and throughout the granule cell layer and had spiny dendrites extending into the external plexiform layer (EPL), consistent with previous observations (Lemasson et al., 2005; Ravi et al., 2015; Sakamoto et al., 2014). For this study, we treated all abGCs as one group, without further subdivision.

We first imaged odor-evoked responses in anesthetized mice because repeated presentation of odors to awake mice has been shown to cause changes in odor-evoked responses across days (Kato et al., 2012). We measured responses in abGC dendrites since GC release sites are located on dendritic spines, and dendritic activity provides the best indication of how abGCs might be positioned to influence the circuit. We first examined abGCs that were several weeks old (>35 days post injection [dpi]). For each experiment, morphology was simultaneously recorded in the red channel during odor presentation to aid in region of interest (ROI) identification and image alignment (Figure 1E). Image stacks were taken during each session to confirm that the imaged dendrites belonged to abGCs (Movie S1).

One of three odor sets was used for all experiments, denoted as odor set A (which contained 20 monomolecular odors), odor set B (8 monomolecular odors and 1 mixture), or odor set C (7 of the monomolecular odors from set B) (Table S1). Odor stimulation led to robust and reliable odor-evoked fluorescence changes in some of the dendrites in any imaged region. Responses were odor specific, and different dendrites could have different odor selectivity (Figure 1F). These data represent some of the first real-time functional responses from abGC dendrites.

AbGCs Can Respond to Odors Soon after Their Arrival

With the knowledge that odor-evoked responses can be readily detected in abGCs, we next sought to determine when, after arrival in the OB (which begins about 3 days after RMS injection), these neurons become responsive to odors. We were able to locate labeled abGCs in the OB starting as early as 6 dpi using the signal in the red channel (Figure S2A). Some neurons at this stage had fully elaborated dendritic trees in the EPL, while others were still growing apical dendrites. Remarkably, we were able to detect responses to odors in the EPL dendrites of these very young abGCs. These cells already had clearly identifiable spines/gemmules and could respond robustly to a variety of odors. Different dendrites of the same abGC had similar responses, suggesting that these were global, cell-wide responses and not just local dendritic responses (Figures S2A–S2C). Though many cells already responded to odors at 6 to 8 dpi (Figures S2D–S2F), we could image a larger population of cells at 9 to 10 dpi, when more labeled cells had arrived in the OB and elaborated dendrites in the EPL. Again, we found that young cells responded robustly to odors (Figure 2A; more below). Our data show that abGCs can respond to odors soon after they arrive in the OB and extend their dendritic trees.

Population-Level Differences in Responses of Young and Mature abGCs

Having described the responses of young abGCs (6–10 dpi), we next asked how their response properties (including magnitude, time course, and stimulus selectivity) change as they develop. Following lentivirus injection in the RMS, we imaged responses to a panel of odors in separate populations of abGC dendrites at different times following injection, young dendrites at 7–10 dpi and more mature dendrites at 35–45 dpi (Figures S5A and S5B). These data should be considered a sample from a population of dendrites rather than cells since some dendrites were from the same cell (although on average, we estimated that only between one and two dendrites from the same cell were included in each field of view, see STAR Methods); more detailed single-cell analysis follows below. We chose to focus on dendritic imaging for most of our experiments since somatic imaging misses a significant fraction of responses, which could be recorded only in the dendrites (Figures S3A–S3D). Nevertheless, our key results were also confirmed by imaging of abGC somata (Figures S3E and S3F).

We found that the response time course of abGC dendrites was diverse at both ages, and dimension reduction methods (principal components analysis) indicated that this temporal diversity could be well described by a few underlying components (Figure 2B). There were no significant differences in the time course of responses between young and mature cells ($p = 0.11$). There was also no difference between the two populations in the variability of responses across multiple repetitions of the same odor (Figure S5H; median CV = 39.5% across median 3 ± 0.7 repetitions SD [young], 43.0% across median 3 ± 0.6 SD repetitions [mature], $p = 0.37$, Wilcoxon rank-sum test). Based on these observations, for subsequent analyses comparing response magnitudes, we characterized the response of abGCs by calculating the average fluorescence change in a 5 s window following odor onset across an average of three repetitions.

We next examined the distributions of responses for all dendrite-odor pairs at the two ages and found that these distributions were significantly different (uncorrected $p = 3.10e{-}38 < 0.001/9$, Kolmogorov-Smirnov test with Bonferroni-corrected threshold for multiple comparisons), with dendrite-odor pairs from young cells exhibiting more responses at higher amplitudes (Figure 2C). This difference was not due to changes in imaging conditions since the noise distributions calculated from trials where no odor was presented were not different ($p = 0.08$, Kolmogorov-Smirnov test) (Figure 2C, inset; Figures S5C–S5G). Young cells had higher median responses to most of the tested odors (Figure 2D) (from top left: uncorrected $p = 1.87e{-}11 < 0.001/9$, 0.60, $6.25e{-}10 < 0.001/9$, $4.60e{-}05 < 0.001/9$, 0.08, $1.62e{-}10 < 0.001/9$, 0.06, 0.02, $5.69e{-}19 < 0.001/9$, Wilcoxon rank-sum test with Bonferroni-corrected thresholds). We found similar differences between the responses of young and mature abGC dendrites, regardless of the amount of recovery time after the cranial window surgery and the inflammatory status of the OB (Figure S4).

To characterize the responses across our odor panel for young versus mature abGC dendrites, we rank ordered the responses to different odors for each dendrite, arranging them from largest positive to largest negative amplitudes (Figure 2E). We found that young abGCs, on average, had significantly larger responses to the top seven ranked odors out of nine in set B (from ranked odor index 1: uncorrected $p = 7.24e{-}21 < 0.001/9$, $2.25e{-}21 < 0.001/9$,

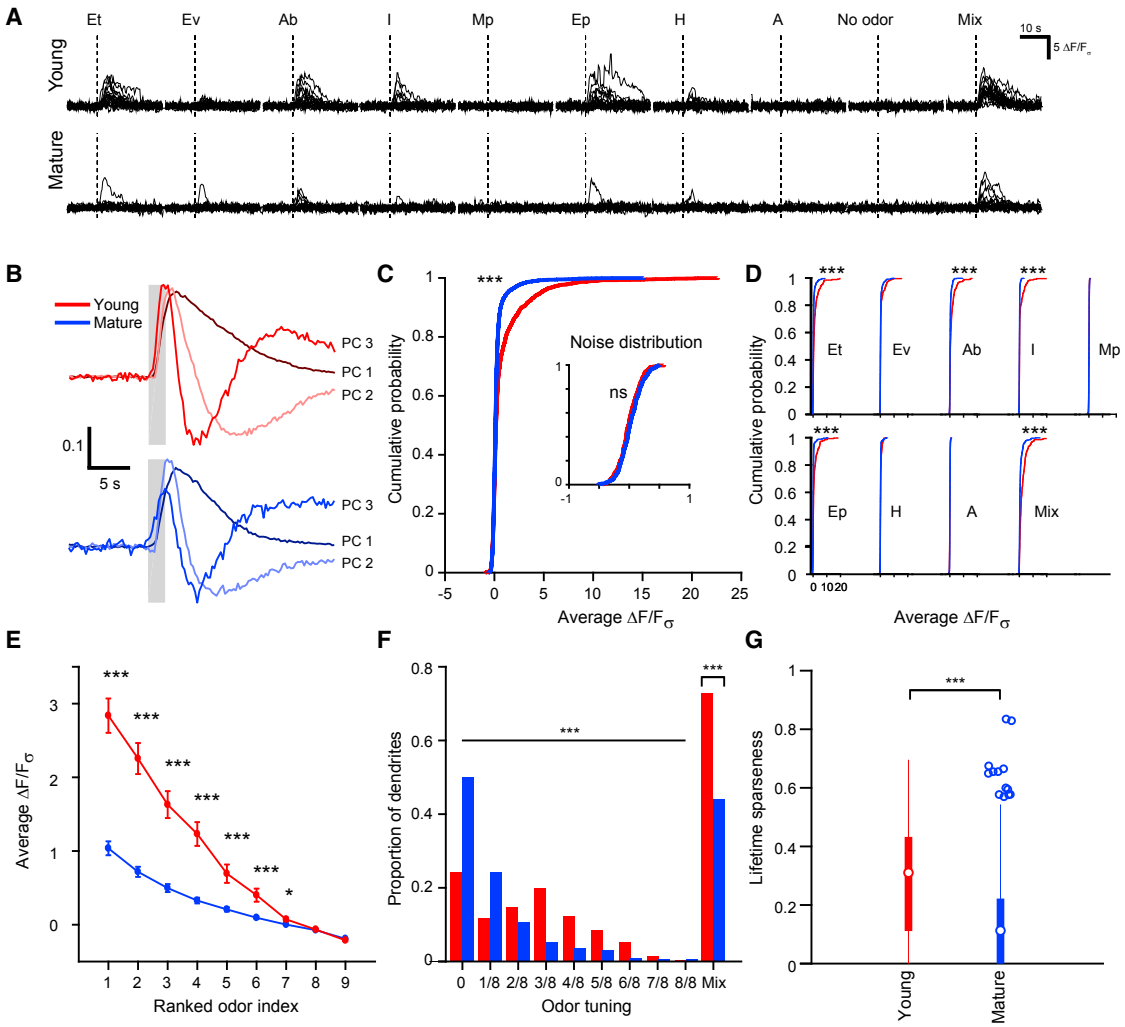

Figure 2. Population-Level Differences in Responses of Young and Mature abGCs

(A) Average traces ($\Delta F/F_\sigma$, GCaMP6s) across 3–5 trials (individual trial traces median filtered over three frames before averaging for presentation) for ten randomly chosen young and mature abGCs to all odors in set B.

(B) The first three principal components (PCs) obtained from PCA of the temporal profiles of responses of all abGC dendrites ($\Delta F/F_\sigma$ traces, GCaMP6s) to all odors in set B. Percent variance explained, young abGCs: 71.9%, 6.1%, and 1.9% and mature abGCs: 37.3%, 5.7%, and 2.3% for the first three PCs, respectively. Shading indicates the odor presentation period (2 s).

(C) Cumulative distributions for average $\Delta F/F_\sigma$ values across repetitions for all dendrite-odor pairs taken over 5 s following odor presentation for young and mature cells. Inset: cumulative distributions for the same measure in no odor trials. Kolmogorov-Smirnov test.

(D) Cumulative distributions for average $\Delta F/F_\sigma$ values across repetitions all dendrites for each odor in set B. Wilcoxon rank-sum test.

(E) For each dendrite, its responses to all odors were ranked by amplitude, and these curves were averaged across all dendrites for each odor. Values are ±SEM. Wilcoxon rank-sum test.

(F) Proportion of dendrites responding above threshold (threshold = 0.4) for the given number odors, not including the mixture, which is shown separately. Chi-square goodness of fit test for proportion of cells with each number of responses out of the eight monomolecular odors and separate chi-square test for proportion of cells responding to the mixture.

(G) Distribution of lifetime sparseness for young and mature cells, where 0 indicates no responses and 1 indicates equal responsiveness to all odors. Boxes represent the 25th to the 75th percentile, whiskers represent 1.5 times the interquartile range, and dots represent points beyond 1.5 times the interquartile range. The white circle in the middle of each box is the median. Wilcoxon rank-sum test.

Data were acquired from 256 young and 405 mature dendrites in 7 mice, imaged with GCaMP6s and odor set B.

*p < 0.05; **p < 0.01; ***p < 0.001.

3.37e−18 < 0.001/9, 1.52e−12 < 0.001/9, 1.86e−08 < 0.001/9, 9.24e−07 < 0.001/9, 0.002 < 0.05/9, 0.38, 0.94, Wilcoxon rank-sum test with Bonferroni-corrected thresholds), indicating that young abGCs respond more broadly to odors (Figure 2F). Importantly, mature abGC dendrites had similar response properties to resident GC dendrites (Figures S5I and S5J), consistent with

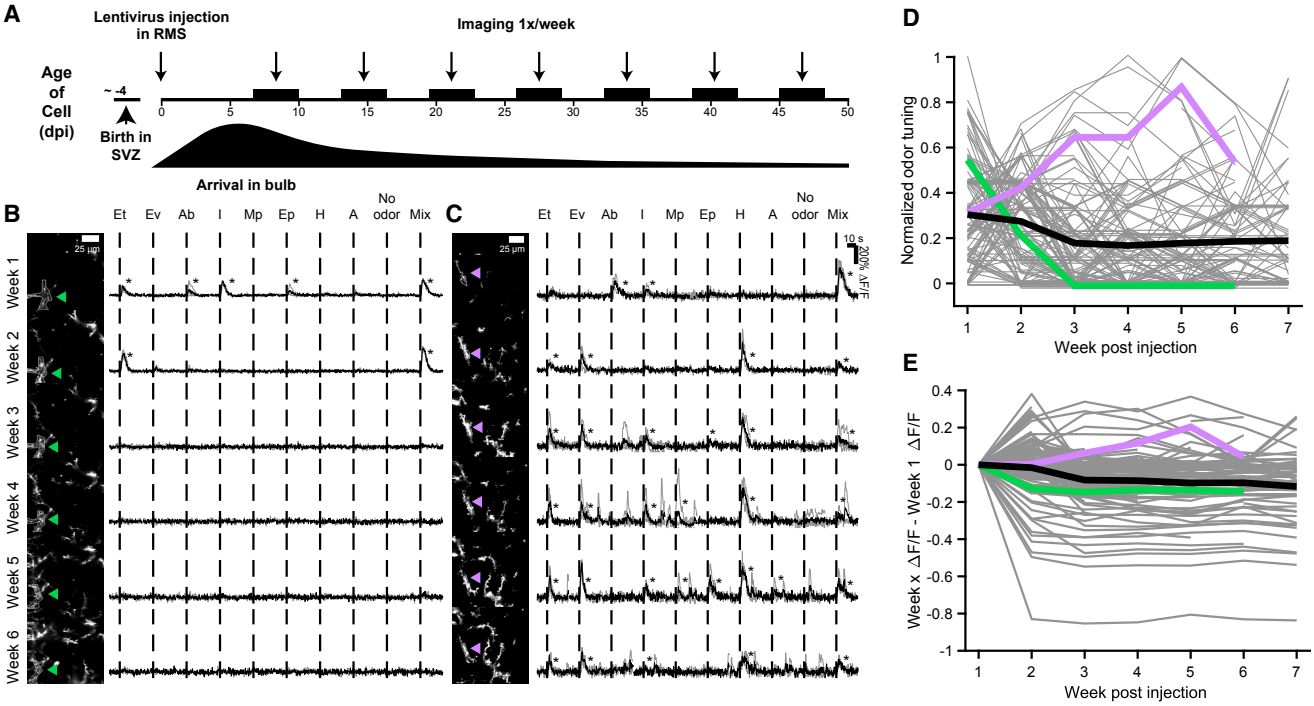

Figure 3. Tracking Individual abGCs as They Undergo Functional Refinement

(A) Experimental timeline. Cells are born in the SVZ and RMS and reach the bulb beginning approximately 1 week later. Cells to be tracked were chosen on the first day of imaging at 7–9 dpi, and subsequent imaging sessions were approximately 1 week apart.

(B) Left: example of a dendrite (ROI outlined in white and highlighted with arrowhead, shown on the average intensity projection from the first trial) that was tracked over 6 weeks. Right: ΔF/F traces (GCaMP6s, odor set B) for this dendrite, which lost some of its initial responses between weeks 1 and 2 and the rest between weeks 2 and 3.

(C) Example of a dendrite from a different field of view that was tracked over 6 weeks (GCaMP6s, odor set B) that dynamically gained and lost responses, with broadest tuning on week 5.

(D) Normalized odor tuning (number of odors that evoked a significant response divided by the number of odors presented) of all followed dendrites (each from a unique cell) over all weeks they were imaged.

(E) For each dendrite, the difference between its average amplitude over responses to all odors on each week and the first week is plotted.

For (D) and (E), data from the example dendrites from (B) and (C) are highlighted in corresponding colors, and the mean is plotted in black.

Data were acquired from a total of 149 dendrites, each traced to a unique cell, in 6 mice. Images are cropped from the entire the field of view.

*, average odor response above threshold.

sparse representation of odors by GCs in anesthetized animals (Kato et al., 2012; Miyamichi et al., 2013; Wienisch and Murthy, 2016).

We also used another measure of odor selectivity that is robust to changes in response amplitude. Considering only whether responses were above or below a threshold (threshold calculated based on an area under the curve analysis of responses at both ages compared to no odor trials) revealed that the distribution of response categories was significantly different in young versus mature abGC dendrites ($p = 1.40e{-}45$, chi-square goodness of fit test) with the distribution for young dendrites shifted toward responses to more odors. In addition, a significantly higher proportion of young dendrites responded to the mixture ($p = 1.34e{-}33$, chi-square test for proportions). We also calculated a different, widely used measure, lifetime sparseness (Wienisch and Murthy, 2016; Willmore and Tolhurst, 2001), to further characterize the breadth of cells' tuning curves across weeks (a high lifetime sparseness score indicates similar responses across odors and a low score indicates a sparser representation with greater stimulus selectivity). Again, by this measure, young dendrites had a sparser odor representation ($p = 7.64e{-}17$, Wilcoxon rank-sum test) (Figure 2G). This analysis suggests that responses in mature abGCs are not just scaled down compared to those in young abGCs but instead represent functional refinement from broad, nonselective odor tuning to a narrower representation. To further investigate this process of functional refinement, we turned to single-cell analysis.

Tracking Identified abGCs over Weeks

There is some uncertainty in the exact age of neurons imaged at later time points since new abGCs could appear at variable times after the injection if they differentiate later or migrate more slowly. Although the rate of such delayed appearance is low (Livneh and Mizrahi, 2011; Mizrahi, 2007), it could bias the analysis of response progression, especially if young abGCs respond very differently from mature abGCs, as suggested by our population data. To overcome this limitation, and to gain additional insights into the process of abGCs' functional refinement at the

single-cell level, we developed methods to track individual abGCs over many weeks *in vivo* (Figure 3A). Here the early high expression of our lentiviral system combined with sparse labeling allowed the repeated identification of individual abGC dendrites using dTomato fluorescence and the overall structural features within an imaged area.

As described above, young abGCs (6–10 dpi) already could respond to odors robustly. The same dendrites could be located a week later and odor responses recorded again (Movies S2 and S3). Importantly, imaging conditions remained stable, ROIs could be accurately tracked throughout the experiment, and there was no correlation between the structural similarity of an ROI from week to week and the degree of response change (Figures S6A–S6C).

In many cells, odor responses recorded early on disappeared completely at a later stage (Figure 3B); however, other cells maintained or increased their responses (Figure 3C). Responses to different odors could be differentially altered in a given abGC, suggesting that responses are not altered exclusively by cell-intrinsic properties (Figure 3C). On average, abGCs' normalized odor tuning (number of responses above threshold divided by the number of odors) and response amplitudes decreased over time (Figures 3D and 3E, solid black lines), corroborating the population studies described above.

We leveraged our ability to track single cells to investigate the stability of responses from week to week, which was not possible in previous studies that monitored populations of adult-born neurons (Danielson et al., 2016; Livneh et al., 2014; Quast et al., 2017). We plotted the responses of all dendrite-odor pairs at successive ages (Figure 4A). If responses were merely scaled down during maturation, the points would lie along a line whose slope depends on the degree of response scaling. Instead, many points lie far from a single unity line, outside the region representing normal response variability (shown by the light gray area in Figure 4A). Responses that were below the dotted lines (representing the threshold for a significant response) on one of the 2 weeks represent responses that were completely eliminated or, less commonly, new responses that appeared from 1 week to another. This can be visualized directly by dividing dendrite-odor pairs' responses from week to week into four categories: "no response" (response below threshold on both weeks), "disappeared" (response above threshold on the first week and below the next week), "appeared" (response below threshold on the first week and above the next week), and "stable" (above threshold for both weeks) (Figure 4B). The fraction of dendrite-odor pairs with responses that disappeared was significantly higher early in the cells' maturation ($p = 0.024$ for weeks 1–2 compared to 6–7, Cochran-Mantel-Haenszel test). The fractions with new or stable responses decreased slightly, but not significantly different, across weeks ($p = 0.12$, "appeared" weeks 1–2 versus 6–7, $p = 0.19$ "stable," weeks 1–2 versus 6–7). For the fraction of responses that was maintained across weeks (between 10%–20% from Figure 4B), we wondered whether there was a change in response amplitude. We plotted the ratio of cell-odor pairs' amplitudes on 1 week compared to the next week for all responses that were maintained across each pair of weeks (Figure 4C). We found that, on average, responses that were maintained did not change in amplitude ($p > 0.05$ for all pairs of weeks, bootstrapped confidence intervals on the mean amplitude ratio). These results are robust to the choice of thresholds used to define responses (Figure S6).

Refinement of Odor Responses in Individual abGCs

After considering dendrite-odor pairs independently, we next wondered how dendrites' tuning curves across all odors change with maturation. Our diverse stimulus panel (20 odors in odor set A, 9 odors in set B) often evoked responses in dendrites to more than one odor, increasing discriminability of tuning curves among dendrites and over time. Consistent with our population data, we found that the ranked responses of dendrites on the first week of imaging were significantly greater than the ranked responses on the last week of imaging (Figure 4D) (GCaMP5: ranked odors 1–3, $p < 0.001/20$, ranked odor 4, $p < 0.01/20$, ranked odors 5–6, $p < 0.05/20$, Wilcoxon signed rank test with Bonferroni-corrected thresholds, n = dendrites from 33 cells imaged on the first and last weeks in 3 mice. For GCaMP6s: ranked odor 1, $p < 0.001/9$, ranked odor 2, $p < 0.01/9$, ranked odors 3–4, $p < 0.05/9$, Wilcoxon signed rank test with Bonferroni-corrected thresholds, n = dendrites from 68 cells imaged on the first and last weeks in 3 mice.).

To quantify the stability of dendritic tuning curves, we plotted the "tuning similarity," which is equal to one minus the Hamming distance between individual dendrites' thresholded tuning curves during successive weeks. Tuning similarity increased during the first few weeks before reaching a plateau (Figure 4E; $p = 1.15e{-}05$, Wilcoxon rank-sum test, n = dendrites from 117 cells for weeks 1–2 and 63 cells for weeks 6–7). This increase in the stability of cells' tuning curves was mostly a consequence of abGCs losing responses over the first few weeks since shuffled data showed a similar increase (Figure 4E). Importantly, the tuning similarity was always greater for the real data than the shuffled data (all $p < 1.0e{-}18$, Wilcoxon rank-sum test), indicating that dendritic tuning curves were more stable than predicted by chance.

We next wondered whether dendrite-odor pairs behave independently, that is whether a given response is equally likely to be lost or maintained, regardless of the behavior of other responses belonging to the same dendrite. To quantify this, we calculated the conditional probability that a response would appear or disappear based on its presence in the previous week (considering the behavior of all dendrite-odor pairs were they all independent) and then constructed predicted tuning curves for dendrites on the second week. We could then quantify whether dendrites lost or gained more responses than predicted if all responses behaved independently. In fact, dendrites tended to fall into one of three regimes during the first 2 weeks: losing more responses, gaining more responses, or remaining more stable than predicted (Figures S6D and S6E). This suggests that functional subpopulations of dendrites behave differently during maturation. Plotting the odor tuning of each dendrite at the beginning and end of imaging revealed that while the odor tuning of a majority of dendrites tended to narrow during maturation (51.5%, n = dendrites from 101 cells in 6 mice), odor tuning broadened for a smaller fraction (15.8%) of cells. The remaining 32.7% of dendrites had odor tuning that was not significantly different

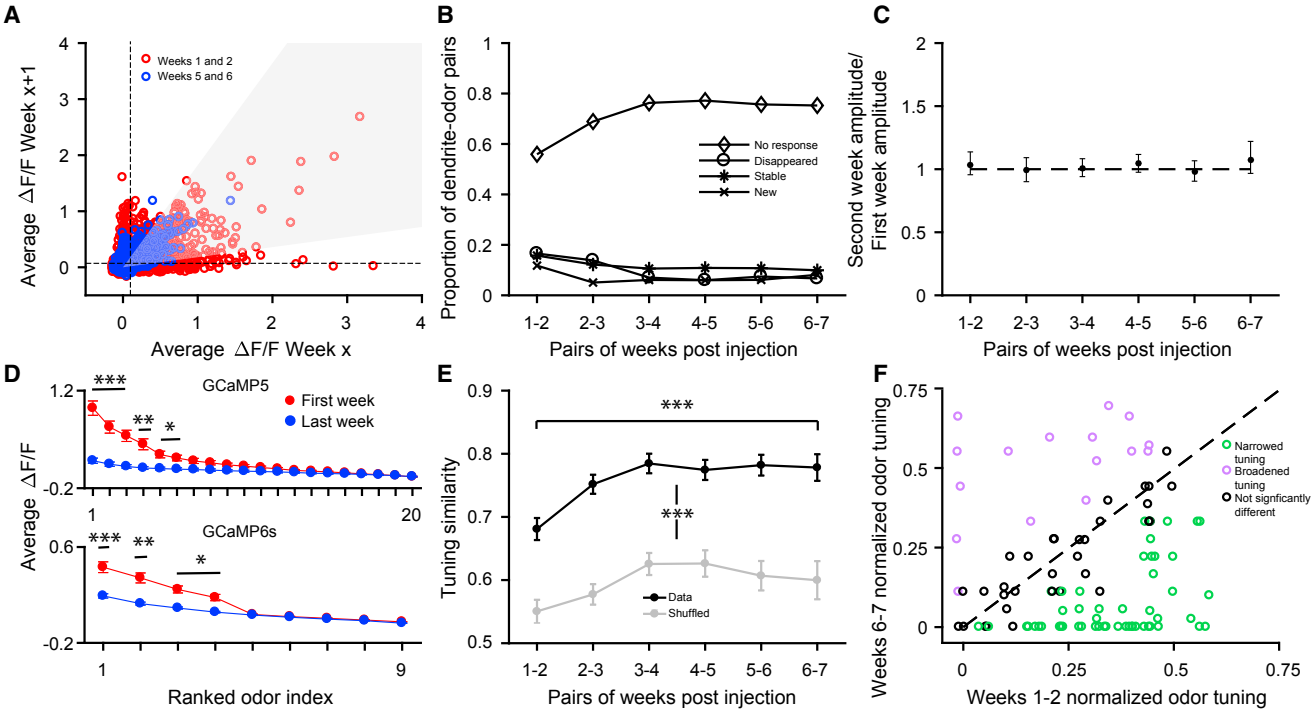

Figure 4. Heterogeneity among abGCs during Functional Refinement

(A) Scatterplot showing responses for all dendrite-odor pairs for two pairs of early weeks (red; week 1, x axis, versus week 2, y axis, and week 2, x axis, versus week 3, y axis) and later weeks (blue; week 5 versus 6 and week 6 versus 7). Shaded light gray area represents the area in which a response on week 2 would fall if its response was within two standard deviations of its response on week 1 with the coefficient of variation taken to be the average from the population dataset, 41.4%. Dotted lines represent the threshold for a significant response.

(B) All dendrite-odor pairs were divided into one of four categories based on whether a response was above threshold (GCaMP5 threshold = 0.1, GCaMP6s threshold = 0.07) on both weeks ("stable"), 1 week ("disappeared" or "new"), or neither of the weeks ("no response").

(C) For all responses above threshold on 2 consecutive weeks, the mean ratio of their amplitudes on the second week in each pair compared to the first week was plotted. Error bars represent the bootstrapped 95% confidence interval for each ratio. A ratio of 1 (no change in amplitude between weeks) is shown with the dotted line.

(D) Ranked odor curves averaged across all dendrites for each odor in set A (GCaMP5) or set B (GCaMP6s) on the first (week 1 or 2) and last (week 6 or 7) week of imaging. Values are mean ± SEM. Comparison between first and last week, Wilcoxon rank-sign test with Bonferroni multiple comparisons correction.

(E) The tuning similarity was calculated for the tuning curve of each dendrite between pairs of weeks and the average across all dendrites plotted ("Data"). For the shuffled data, the responses for all dendrite-odor pairs on each week were shuffled (keeping the total number of responses the same), and the same measure was calculated. The mean across 1,000 shuffles is plotted. Error bars are ±SEM. Wilcoxon rank-sum test.

(F) The normalized odor tuning (number of odors with a significant response divided by total number of odors in the set) averaged across weeks 1–2 for each dendrite is plotted against its tuning averaged across weeks 6–7. Colors represent dendrites whose tuning on weeks 6–7 significantly differed from its tuning on weeks 1–2. Points are jittered to make overlapping points visible.

Data were acquired from the same 149 dendrites as in Figure 3.

*$p < 0.05$; **$p < 0.01$; ***$p < 0.001$.

between the first and last imaging sessions (Figure 4F). These results suggest that there is heterogeneity among dendrites' patterns of functional maturation, with most dendrites losing some or all of their initial responses but a subpopulation tending to maintain existing responses and/or gain new responses.

We took advantage of occasional late-arriving abGCs to ask whether cells' response properties relate to the time of injection in the RMS. When imaging a field of view, new dendrites could sometimes be identified at a later time point, and some of them could be traced to newly arriving cells (Figures 5A and 5B). We found that dendrites belonging to these late-arriving cells, which we termed "newcomers," seemed to undergo a similar process of functional refinement as abGCs arriving in the first wave of migration (Figures 5C–5E). Altogether, the newcomers more closely resembled abGCs imaged in the first week after RMS injection than more mature abGCs imaged at the time of arrival of the newcomers in both odor tuning and response amplitude (for both tuning and amplitude, 89% of newcomers were above the mean for their date of appearance and 71% were above the mean for the first week of imaging). The ranked response amplitudes of newcomers in the first imaging session after they appeared were not significantly different from abGCs imaged on the first week after injection (Figure 5F; all $p > 0.05/20$ [GCaMP5] or $p > 0.05/9$ [GCaMP6s], Wilcoxon rank-sum test with Bonferroni multiple comparisons correction). These data indicate that the date of arrival in the OB dictates initial response amplitude and the beginning of functional refinement rather than date of infection.

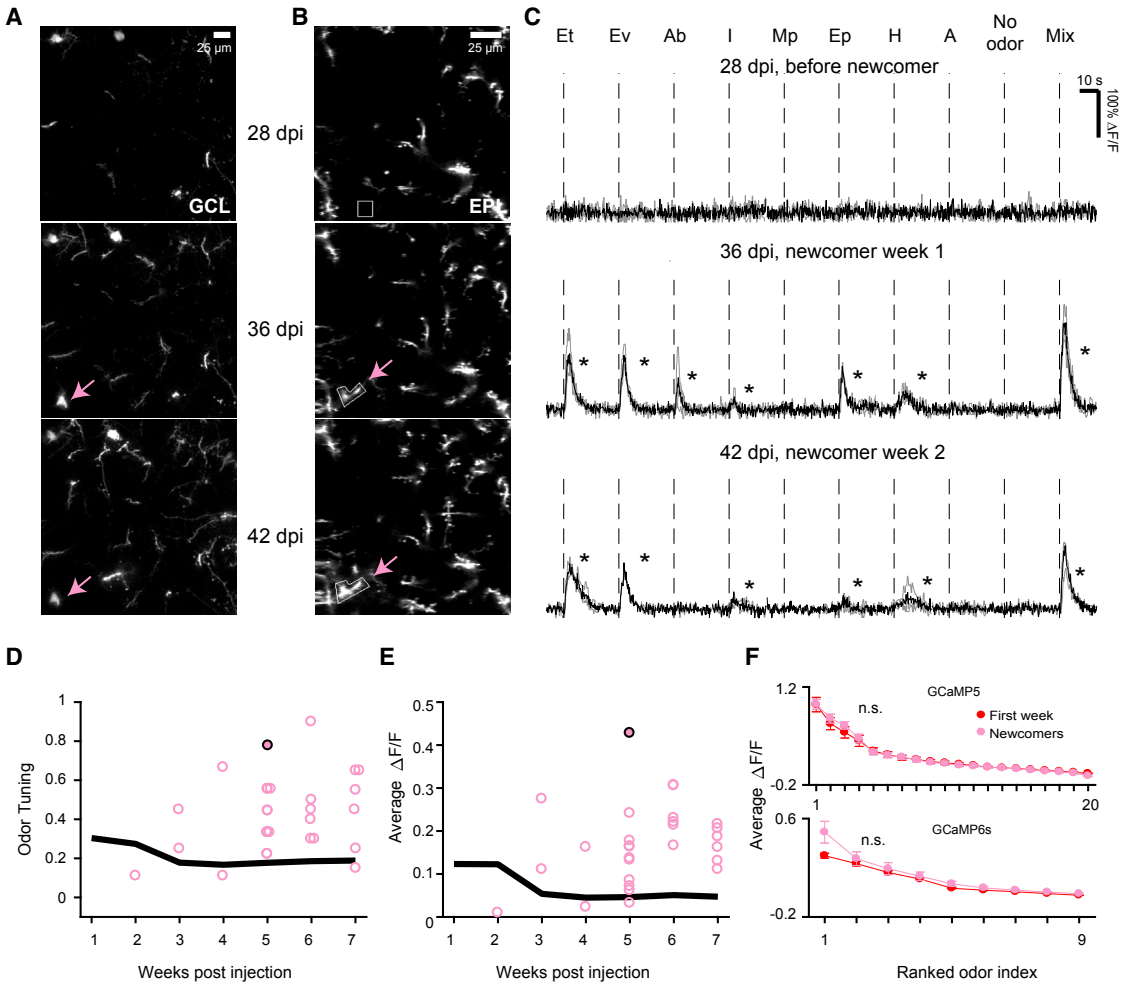

Figure 5. Newcomers Undergo a Similar Pattern of Functional Refinement as Early-Arriving abGCs

(A) Maximum-intensity projection of 24 µm taken from z stacks showing cell bodies in the GCL at 28, 36, and 42 dpi. A newcomer cell appeared on 36 dpi (pink arrow).

(B) Average-intensity projection of an imaging field in the EPL at 28, 36, and 42 dpi showing a newcomer dendrite (pink arrow) that that was traced to the soma in (A), with the analysis ROI outlined in white.

(C) ΔF/F traces (GCaMP6s, odor set B) for the newcomer dendrite, starting the week before it appeared (no responses), the first week it appeared, and 1 week later at 28, 36, and 42 dpi, respectively, showing that its tuning was broadest on the first week that it appeared.

(D) Odor tuning for each newcomer cell is plotted on the week that it appeared (points are jittered to make overlapping points visible). The overall mean tuning of all abGCs is shown by the black line (replotted from Figure 3D). The example from (C) is shown with a filled circle.

(E) Average response amplitude of each newcomer cell is plotted on the week that it appeared, along with the overall mean of all cells (black line). The example from (C) is shown with a filled circle.

(F) Ranked odor curves for dendrites on the first week of imaging (replotted from Figure 4D) compared to that of newcomers on the first week they appeared, plotted separately for cells imaged with GCaMP5/odor set A or GCaMP6s/odor set B. Wilcoxon rank-sum test with Bonferroni multiple comparisons correction. Values are ±SEM.

Data were acquired from 28 newcomer dendrites, each traced to a unique cell, 14 each with GCaMP5/odor set A and GCaMP6s/odor set B in 3 mice each. Images are cropped from the entire the field of view.

*, average odor response above threshold.

To provide further evidence that the changes in abGC responses that we observed were not due to increasing expression of reporters, repeated imaging, or some other aspect of our experimental paradigm, we performed a control experiment. We suppressed expression of reporters with doxycycline until several months after viral injection and then watched the evolution of responses in resident GCs, labeled via injection into the OB, using the same imaging paradigm as before. This way, when expression of GCaMP began, these GCs were at least 12 weeks old. We found that initial responses imaged 1 week after doxycycline removal had similar amplitudes to responses in mature abGCs imaged 7 weeks after injection ($p > 0.05/20$, Wilcoxon rank-sum test with Bonferroni-corrected threshold) and that the odor tuning of these cells was more stable across weeks

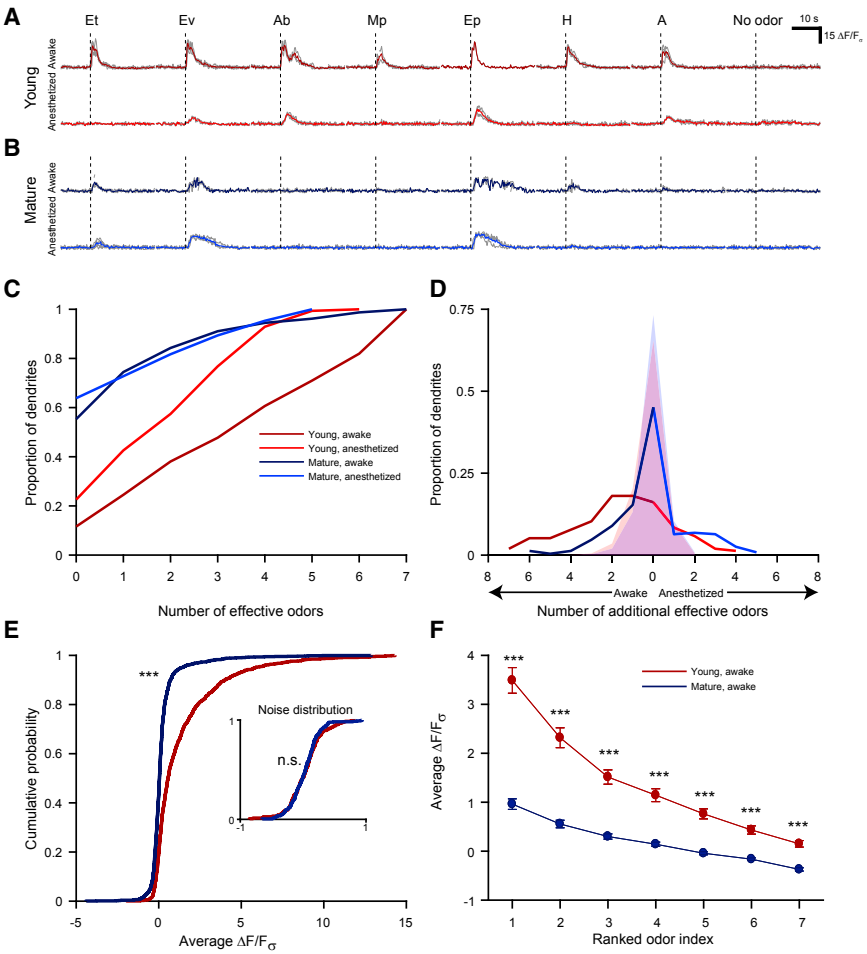

Figure 6. Young abGCs' Responsiveness Is Enhanced in the Awake State

(A) Example traces ($\Delta F/F_\sigma$, GCaMP6s) from a young abGC imaged in the awake and then the anesthetized state to the odors in set C. Average trace shown in color and individual repetitions in gray.

(B) Example traces from a mature abGC imaged in the awake and then the anesthetized state.

(C) The cumulative distribution of effective odors (odors that evoked responses above threshold, 0.48) to activate young and mature abGCs in the awake and anesthetized states.

(D) The difference in the number of effective odors between the awake and anesthetized states was calculated for each dendrite. The probability distribution across all dendrites is plotted (lines). Shaded areas show the expected distributions across 1,000 simulations of how odor tuning for each dendrite could change based on the CV in the awake state (median CV young = 0.40, median CV mature = 0.36).

(E) Cumulative distributions for average $\Delta F/F_\sigma$ values across repetitions for all dendrite-odor pairs taken over 5 s following odor presentation for young and mature dendrites in awake mice. Inset: cumulative distributions for the same measure in no odor trials. Kolmogorov-Smirnov test with Bonferroni-corrected threshold.

(F) For each dendrite, its responses to all odors in awake mice were ranked by amplitude, and these curves were averaged across all dendrites for each odor. Values are ±SEM. Wilcoxon rank-sum test with Bonferroni multiple comparisons correction. Data were acquired from 152 young and 228 mature dendrites, 4 mice per group, all imaged with GCaMP6s/odor set C.

***p < 1e−14.

(Figures S7A–S7G). Furthermore, electrophysiological analysis indicated that passive and spiking properties of cells expressing GCaMP6s were indistinguishable from those of cells labeled only with dTomato (Figures S7H–S7N).

Taken together, these data indicate that the majority of abGCs lose most or all of their responses during maturation, especially during the first 3 weeks after cell labeling, while maintaining a fraction of their responses to achieve more narrow tuning curves. A small subpopulation (~15% of dendrites) tends to become more broadly tuned during maturation—a result that would not have been visible to population analysis.

Odor Responses of abGCs in Awake Mice

Anesthesia affects olfactory circuits in nuanced ways that may not be equivalent to simple scaling of responses in individual cells (Kato et al., 2012; Otazu et al., 2015). Therefore, we directly compared the responses of young and mature abGC dendrites in the awake versus the anesthetized state to odor set C (Figures 6A and 6B). We found that young abGC dendrites tended to respond to more odors than mature abGC dendrites, and this effect was more dramatic in awake mice (Figure 6C). This was due to individual young abGC dendrites having broader tuning in the awake than the anesthetized state, with a smaller proportion of mature abGC dendrites exhibiting this behavior (Figure 6D). Overall, this resulted in significant differences in the overall response amplitude distributions (Figure 6E) ($p = 3.50e{-}85 < 1e{-}14/7$, Kolmogorov-Smirnov test with Bonferroni-corrected threshold) and ranked odor curves (by ranked odor index: $p = 2.35e{-}27 < 1e{-}14/7$, $2.13e{-}25 < 1e{-}14/7$, $1.53e{-}25 < 1e{-}14/7$, $8.34e{-}22 < 1e{-}14/7$, $4.93e{-}21 < 1e{-}14/7$, $7.13e{-}18 < 1e{-}14/7$, $8.07e{-}16 < 1e{-}14/7$, Bonferroni-corrected thresholds, Wilcoxon rank-sum test) (Figure 6F) of young versus mature abGC dendrites in awake mice.

Odor Enrichment

While the morphological properties, synaptic inputs, and survival rate of abGCs can be modulated by olfactory experience (Dahlen et al., 2011; Kelsch et al., 2009; Lepousez et al., 2014; Yamaguchi and Mori, 2005), less is known about how the functional properties of these cells could be altered. We leveraged our ability to record responses of repeatedly identified individual abGCs to odors across multiple weeks to ask how their responses are altered by experience. We enriched the olfactory environment of mice shortly after viral injection into the RMS by leaving all the odors used in the imaging experiments in small containers within the home cages of mice. This method has been shown

to alter many properties of abGCs in earlier studies (Livneh and Mizrahi, 2011; Livneh et al., 2014; Pallotto et al., 2012; Rochefort et al., 2002) and serves as a starting point for more specific manipulations.

On the first day of imaging, abGC response amplitudes were similar in control and enriched mice; by the second week, however, responses in enriched mice were significantly higher than in control mice and remained elevated for several weeks, eventually returning to control levels by the last week (Figure 7A) (by week: $p = 0.29$, 1.96e−04, 0.002, 0.03, 0.004, 0.02, 0.62, Wilcoxon rank-sum test). Similarly, odor tuning was significantly broader in enriched mice for all weeks after the first week (Figure 7B) (by week: $p = 0.29$, 4.62e−05, 8.94e−05, 0.020, 0.002, 0.023, 0.021). Lifetime sparseness was also significantly higher in enriched mice (Figure 7C) (by week: $p = 0.11$, 8.63e−04, 1.31e−04 0.019, 0.002, 0.02, 0.02, Wilcoxon rank-sum test), suggesting that cells in enriched mice remain broadly responsive for a longer period.

We also asked how the stability of the representation was altered by odor enrichment. Plotting the tuning curve similarity from week to week (Figure 7D) and across all pairs of weeks (Figures 7E and 7F) revealed that this measure was lower in enriched mice after week 1 but eventually increased to control levels by weeks 6 to 7, suggesting more dynamic changes in cells' tuning curves in enriched mice (by week: $p = 0.24$, 0.001, 1.96e−04, 4.90e−04, 0.012, 0.17, Wilcoxon rank-sum test). When we divided the changes in dendrites' tuning curves into categories (Figures 7G and 7H), we found that the rate of appearing and disappearing responses was similar on week 1 and then higher across all pairs of weeks until weeks 6 to 7 in enriched mice ($p > 0.05/20$ for weeks 1–2, $p < 0.001/20$ for weeks 2–3, 3–4, and 4–5 and $p < 0.01/20$ for weeks 5–6, chi-square test with Bonferroni-corrected threshold). The proportion of stable responses was also elevated in enriched mice throughout the experiment, reaching significance for the first three pairs of weeks ($p < 0.001/20$ for weeks 1–2, 2–3, and 3–4, chi-square test with Bonferroni-corrected threshold). These data indicate that enriching the odor environment causes abGCs to remain more responsive and broadly tuned to the enriched odors for a longer period during maturation.

DISCUSSION

We have characterized for the first time *in vivo*, the evolution of stimulus-evoked responses in individually tracked abGCs. We find that, on average, the responsiveness of abGCs decreases as they mature, but a subpopulation of cells becomes more broadly tuned with maturation, indicating functional heterogeneity. Furthermore, the period of heightened odor responses in abGCs is sensitive to sensory experience in the form of olfactory enrichment.

Technical Advances and Caveats

An important technical advance contributed to our ability to measure responses in abGCs beginning shortly after they arrive in the OB and continuing for up to 2 months *in vivo*. The lentiviral system that we used allows for excellent reporter expression due to strong activation of the Tet-responsive promoter while also allowing for sparse labeling (Hioki et al., 2009), which was essential for tracking cells over time. Early high expression allowed us to image cells within a week after their arrival in the OB (compared to 2–3 weeks after arrival, the youngest time point examined previously; Quast et al., 2017) and was essential for our conclusions, because most of the changes in abGC responses occurred in the first 2 weeks after injection. The sparse labeling afforded by our lentiviral system also made it possible to track individual neurons across weeks. Recently described genetic methods (Garcia et al., 2014; Quast et al., 2017) offer the advantage of higher cell yields but produce different expression patterns than bromodeoxyuridine (BrdU) labeling (Yamaguchi and Mori, 2005) and lentiviral injection (Consiglio et al., 2004; Kopel et al., 2009; Lepousez et al., 2014), raising the possibility that they may target subpopulations of abGCs (see more below). The ability to compare an individual cell's responses at different time points removes this concern, and we anticipate that this tool will be useful for future *in vivo* studies of abGCs.

Several potential concerns need to be dispelled to allow appropriate interpretation of our study. Increasing GCaMP expression over time can damage cells and attenuate their responses if expression levels become too high (Tian et al., 2009). However, the fact that resident GCs respond similarly to mature abGCs and the result that resident GCs responded similarly regardless of GCaMP expression level (Figures S5I, S5J, and S7) argue that changes in GCaMP expression are not responsible for the sparsening of responses that we found with abGC maturation. In addition, the relation between GCaMP fluorescence and neuronal activity may vary with neuronal ages. However, calcium handling is reportedly similar in GCs of different ages (Egger and Stroh, 2009), and GCaMP expression does not affect any of the electrophysiological properties of abGCs that have been examined to date (Figure S7; Quast et al., 2017).

Dendritic Imaging

Importantly, our study is the first to measure dendritic responses of abGCs at different ages. Unlike many cell types, where somatic imaging provides a good approximation of input summation, there is evidence that GCs may integrate synaptic inputs locally in the dendrites as well as the soma (Bywalez et al., 2015). This is particularly relevant to olfactory processing since GC release sites are located on dendritic spines, and we found that abGC dendrites are more responsive than somata, consistent with previous work (Wienisch and Murthy, 2016). In this study, we either treated abGC dendrites separately without regard to the cell of origin for population data or averaged across dendrites belonging to a single cell for the single-cell tracking experiments. Future work can further investigate whether local signaling in abGCs changes during maturation.

AbGCs Respond Early and Become More Selective as They Mature

The finding that abGC responses decrease in most cells as they mature in the first few weeks after they are born may be partially explained by changes in intrinsic cellular properties such as input resistance (Carleton et al., 2003; Nissant et al., 2009). However, the fact that some responses disappear completely while others are maintained at similar amplitudes argues that the functional refinement that we observe cannot be completely explained by

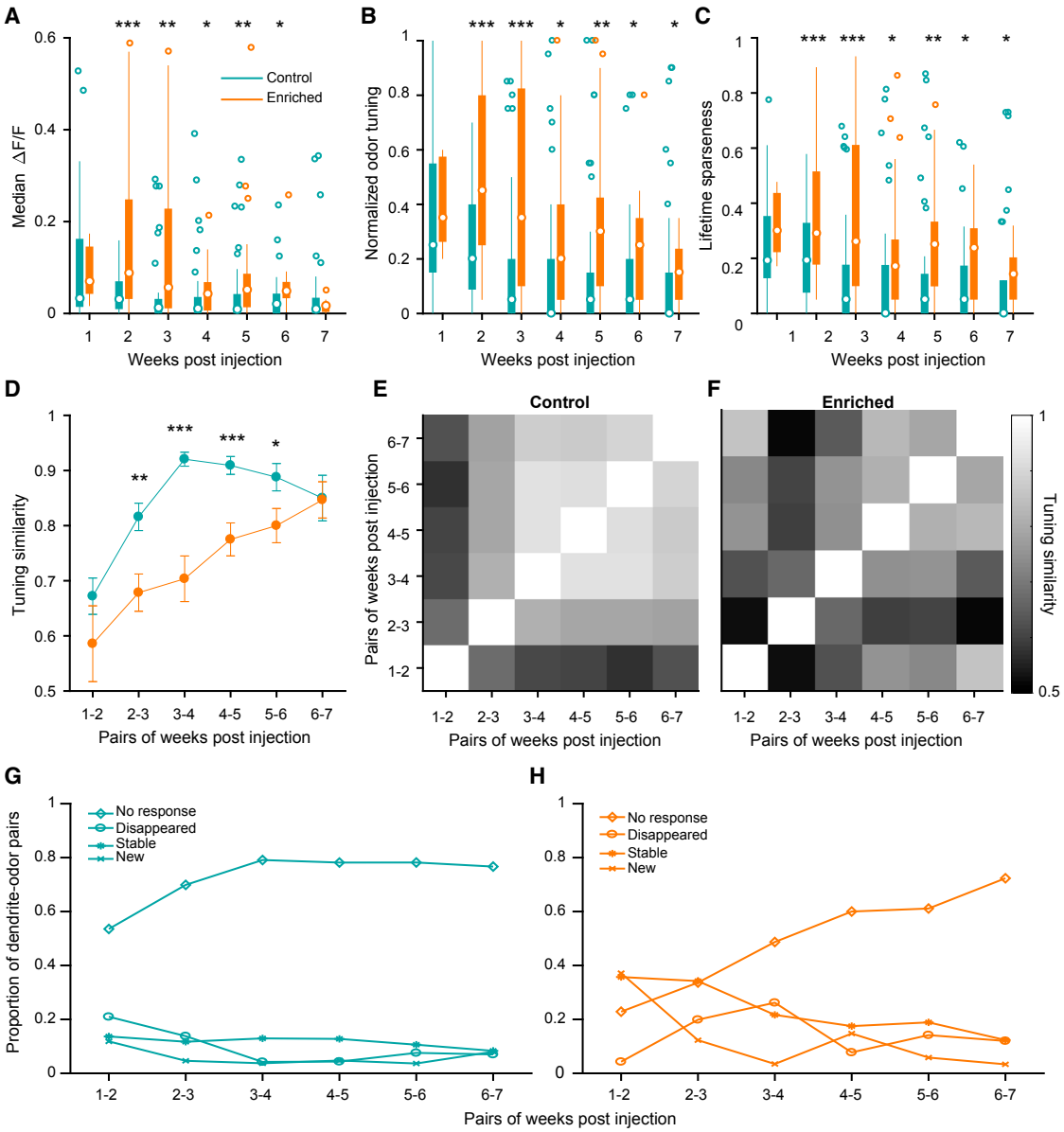

Figure 7. Odor Enrichment Extends Time Window of Increased Excitability and Broad Responsiveness

For panels (A) through (C), boxes represent the 25th to the 75th percentile, whiskers represent 1.5 times the interquartile range, and dots represent points beyond 1.5 times the interquartile range. The white circle in the middle of each box is the median.

(A) Distributions of median ΔF/F for all dendrites 7 weeks after injection. Wilcoxon rank-sum test.

(B) Distribution of odor tuning for all dendrites 7 weeks after injection. Wilcoxon rank-sum test.

(C) Distributions of lifetime sparseness for all dendrites for 7 weeks after injection. Lifetime sparseness was set to 0 for any dendrite with responses below threshold. Wilcoxon rank-sum test.

(D) For sequential pairs of weeks post-injection, the tuning similarity between the tuning curves for a dendrite on the first week compared to the second week was calculated, and the mean of the tuning similarity values for all dendrites was plotted. Values are mean ± SEM. Wilcoxon rank-sum test.

(E) The same analysis as in (D) was performed for all pairs of weeks for dendrites in control mice, and the mean tuning similarity is shown for each pair.

(F) The same plot as in (D) for dendrites in enriched mice.

(G) Control data replotted to show a side-by-side comparison with (H).

(H) For dendrite-odor pairs in enriched mice, response categories were calculated as for Figure 4B.

Data were acquired from 51 dendrites in 3 enriched mice and 41 dendrites in 3 control mice (includes GCaMP5 data from Figure 4), all imaged with GCaMP5/odor set A.

*p < 0.05; **p < 0.01; ***p < 0.001.

such mechanisms. The fact that abGCs have been shown to be capable of generating action potentials by the time of our first imaging sessions at 6–10 dpi (Bardy et al., 2010; Carleton et al., 2003), as well as our observation that activity in young abGCs was typically global and did not differ in time course from that in more mature abGCs, argues against the possibility that responses in young abGCs represent a qualitatively different type of activity than responses in mature abGCs. It is still unclear, however, which synaptic inputs may be contributing to the responses we observed in very young abGCs. The first excitatory inputs abGCs receive are likely to be from cortical feedback fibers (Kelsch et al., 2008; Panzanelli et al., 2009), but there is ultrastructural evidence that abGCs receive glutamatergic synapses (only some of which are reciprocal) in the EPL, from putative mitral cell dendrites as early as 7 dpi (Panzanelli et al., 2009). This leaves open the possibility that either (or both) of these categories of inputs may contribute to the early responses that we observe.

Since most studies suggest that abGCs receive an increasing number of synaptic inputs over time (Kelsch et al., 2008; Pallotto et al., 2012), it is unlikely that large-scale synaptic pruning underlies increasing selectivity of abGC odor responses with maturation. Instead, we suggest that selective synaptic refinement might allow abGCs to become more tuned to a particular glomerular module, allowing them to contribute selective inhibition to the olfactory circuit. This process might be similar to that observed in other classes of adult-born neurons in the OB, such as PG cells, where it was reported that abGCs' responses were correlated with responses in more glomeruli early on compared to later in their development (Livneh et al., 2014).However, PG cells appear to have a delayed profile of functional maturation compared to GCs, with broadest tuning at 4 weeks post-RMS injection (while in our study most abGCs had broadest tuning at 1–2 weeks).

Importantly, our study is the first to image responses of adult-born neurons in the OB in awake animals. We found that, consistent with previous reports of the effects of anesthesia on GC somata (Cazakoff et al., 2014; Kato et al., 2012), abGC dendrites are more responsive and broadly tuned in the awake state. Interestingly, this effect was more pronounced in young abGC dendrites, resulting in a more dramatic difference between young and mature cells in awake mice compared to mice anesthetized with ketamine/xylazine.

Long-Term Functional Monitoring of Individual abGCs

To our knowledge, this is the first study in which adult-born neurons' functional responses have been tracked at a single-cell level *in vivo*. This allowed us to characterize heterogeneity among an individual abGC's response to different odors over time and between abGCs. We found that abGCs' responses do not all change in the same way over time—an individual cell can maintain responses to some odors while losing responses to others. Furthermore, a subset of abGCs behaved differently from the rest of the population, with narrower tuning initially that broadened during development. The morphological and/or molecular correlates of this functional heterogeneity could be investigated in future studies.

Our data support earlier observations that the majority of young abGCs are more responsive to novel stimuli than mature cells, as measured by the less direct, less sensitive method involving immediate early gene expression (Magavi et al., 2005), but contrast with recent observations using Cre lines to target populations of abGCs at different ages that suggested an overall broadening of tuning curves with maturation (Quast et al., 2017). Differences in the populations of cells targeted by lentivirus versus these genetic methods may account for this discrepancy, especially since the distribution pattern of cells across OB layers in these Cre lines (Quast et al., 2017) appears to be inconsistent with the previously described distribution of abGCs, which are distributed uniformly from superficial to deep layers (Figure 1C), in contrast to neonatal-born GCs, which preferentially localize to superficial layers (Lemasson et al., 2005). Since there is evidence that GCs in different layers of the OB may participate in functionally distinct microcircuits (Orona et al., 1983), it will be important to further investigate the maturational patterns that may be specific to particular subpopulations of abGCs.

Critical Periods

Across all tracked abGCs, we found that most changes in responses (either new responses appearing or previously measured responses disappearing) occurred during the first 3 weeks after cell labeling (approximately 4 weeks after their birth) and reached a steady state thereafter. This time frame closely matches the critical period described for synaptogenesis and survival of abGCs (2 to 4 weeks after their birth) (Kelsch et al., 2009; Yamaguchi and Mori, 2005). Interestingly, olfactory enrichment prolonged this period of functional immaturity, with abGCs' responses remaining elevated and broad, and more responses appearing or disappearing in cells in enriched mice for many weeks. This dynamism could represent a greater flexibility of abGCs, allowing them to explore a greater space of inputs in a richer sensory environment.

The period of functional plasticity we have described also corresponds to the time period when the spines of abGCs are most dynamic (Sailor et al., 2016), providing a mechanism for abGCs to sample ongoing circuit activity during the period in which they are highly responsive. Enrichment led to a higher degree of sampling of odor information over a longer time period in our paradigm, which involved uniform enrichment with all odors. Future experiments will be necessary to determine whether enrichment extends the time period of responsiveness across all odors, or only increases responses to those odors used in the enrichment, and whether abGCs become selectively more responsive only to enriched odors.

Implications for Circuit Function

It remains an open question when, in a particular cell's developmental trajectory, that cell begins to contribute to the olfactory bulb network. Although functional synapses appear in some cells by 2–3 weeks after birth (Bardy et al., 2010; Kelsch et al., 2008), the amount of input into the OB network for a given cohort of abGCs increases for up to a month thereafter (Bardy et al., 2010). Since most functional refinement was completed by 3 weeks post-injection in our paradigm, this supports the idea that abGCs follow the rule of "listen before you speak," which is that they sample ongoing network activity before beginning to influence it (Carleton et al., 2003; Kelsch et al., 2008). However, our finding that olfactory enrichment prolonged the time course of

functional refinement offers the possibility that adult-born neurons may provide a greater contribution to olfactory processing in conditions where animals experience more olfactory stimuli.

STAR★METHODS

Detailed methods are provided in the online version of this paper and include the following:

- KEY RESOURCES TABLE
- CONTACT FOR REAGENT AND RESOURCE SHARING
- EXPERIMENTAL MODEL AND SUBJECT DETAILS
- METHOD DETAILS
  - Surgery
  - Viral Vectors
  - Immunohistochemistry
  - *In Vivo* Imaging
  - Imaging in Awake Animals
  - Odor Stimulation
  - Odor Enrichment
  - Electrophysiology
- QUANTIFICATION AND STATISTICAL ANALYSIS
  - In Vivo Imaging Analysis
  - Cranial Window Inflammation Analysis
  - Statistical Tests
- DATA AND SOFTWARE AVAILABILITY

SUPPLEMENTAL INFORMATION

Supplemental Information includes seven figures, one table, and three movies and can be found with this article online at https://doi.org/10.1016/j.neuron.2017.09.039.

AUTHOR CONTRIBUTIONS

All authors contributed to experimental design. J.L.W. and M.W. collected and analyzed the data. J.L.W. and V.N.M. wrote the manuscript.

ACKNOWLEDGMENTS

This work was supported by a grant from the NIH/NIDCD (R01 DC013329) to V.N.M. M.W. was supported by an HFSP long-term fellowship (LT1069) and J.L.W. by the NSF GRFP (DGE1144152) and NRSA (F31 DC016482) from the NIH/NIDCD.

Microscopy on fixed tissue samples was performed at the Harvard Center for Biological Imaging, where J.L.W. was supported by the Simmons Family Award. We thank Renate Hellmiss of MCB Graphics for advice about figure presentation. We thank Takeshi Kaneko and Hiroyuki Hioki for sending plasmids. Pilot experiments were assisted by Nathan Geon-woo Kim, Gautier Breville, and Young-ji (Helen) Cho. We thank Pierre-Marie Lledo for generous advice in the early stages of the project. We also thank the members of our group, in particular, Joseph Zak and Vikrant Kapoor, for productive discussions. Joseph Zak also assisted with electrophysiological recordings.

Received: January 26, 2017
Revised: July 26, 2017
Accepted: September 22, 2017
Published: October 19, 2017

REFERENCES

Adam, Y., and Mizrahi, A. (2011). Long-term imaging reveals dynamic changes in the neuronal composition of the glomerular layer. J. Neurosci. *31*, 7967–7973.

Alonso, M., Lepousez, G., Sebastien, W., Bardy, C., Gabellec, M.-M., Torquet, N., and Lledo, P.-M. (2012). Activation of adult-born neurons facilitates learning and memory. Nat. Neurosci. *15*, 897–904.

Bardy, C., Alonso, M., Bouthour, W., and Lledo, P.-M. (2010). How, when, and where new inhibitory neurons release neurotransmitters in the adult olfactory bulb. J. Neurosci. *30*, 17023–17034.

Bywalez, W.G., Patirniche, D., Rupprecht, V., Stemmler, M., Herz, A.V., Pálfi, D., Rózsa, B., and Egger, V. (2015). Local postsynaptic voltage-gated sodium channel activation in dendritic spines of olfactory bulb granule cells. Neuron *85*, 590–601.

Carleton, A., Petreanu, L.T., Lansford, R., Alvarez-Buylla, A., and Lledo, P.-M. (2003). Becoming a new neuron in the adult olfactory bulb. Nat. Neurosci. *6*, 507–518.

Cazakoff, B.N., Lau, B.Y.B., Crump, K.L., Demmer, H.S., and Shea, S.D. (2014). Broadly tuned and respiration-independent inhibition in the olfactory bulb of awake mice. Nat. Neurosci. *17*, 569–576.

Chow, S.F., Wick, S.D., and Riecke, H. (2012). Neurogenesis drives stimulus decorrelation in a model of the olfactory bulb. PLoS Comput. Biol. *8*, e1002398.

Consiglio, A., Gritti, A., Dolcetta, D., Follenzi, A., Bordignon, C., Gage, F.H., Vescovi, A.L., and Naldini, L. (2004). Robust in vivo gene transfer into adult mammalian neural stem cells by lentiviral vectors. Proc. Natl. Acad. Sci. USA *101*, 14835–14840.

Dahlen, J.E., Jimenez, D.A., Gerkin, R.C., and Urban, N.N. (2011). Morphological analysis of activity-reduced adult-born neurons in the mouse olfactory bulb. Front. Neurosci. *5*, 66.

Danielson, N.B., Kaifosh, P., Zaremba, J.D., Lovett-Barron, M., Tsai, J., Denny, C.A., Balough, E.M., Goldberg, A.R., Drew, L.J., Hen, R., et al. (2016). Distinct contribution of adult-born hippocampal granule cells to context encoding. Neuron *90*, 101–112.

Dubbs, A., Guevara, J., and Yuste, R. (2016). moco: fast motion correction for calcium imaging. Front. Neuroinform. Published online February 16, 2016. https://doi.org/10.3389/fninf.2016.00006.

Egger, V., and Stroh, O. (2009). Calcium buffering in rodent olfactory bulb granule cells and mitral cells. J. Physiol. *587*, 4467–4479.

Garcia, I., Quast, K.B., Huang, L., Herman, A.M., Selever, J., Deussing, J.M., Justice, N.J., and Arenkiel, B.R. (2014). Local CRH signaling promotes synaptogenesis and circuit integration of adult-born neurons. Dev. Cell *30*, 645–659.

Gratzner, H.G. (1982). Monoclonal antibody to 5-bromo- and 5-iododeoxyuridine: a new reagent for detection of DNA replication. Science *218*, 474–475.

Hioki, H., Kuramoto, E., Konno, M., Kameda, H., Takahashi, Y., Nakano, T., Nakamura, K.C., and Kaneko, T. (2009). High-level transgene expression in neurons by lentivirus with Tet-Off system. Neurosci. Res. *63*, 149–154.

Kato, H.K., Chu, M.W., Isaacson, J.S., and Komiyama, T. (2012). Dynamic sensory representations in the olfactory bulb: modulation by wakefulness and experience. Neuron *76*, 962–975.

Kelsch, W., Lin, C.-W., and Lois, C. (2008). Sequential development of synapses in dendritic domains during adult neurogenesis. Proc. Natl. Acad. Sci. USA *105*, 16803–16808.

Kelsch, W., Lin, C.-W., Mosley, C.P., and Lois, C. (2009). A critical period for activity-dependent synaptic development during olfactory bulb adult neurogenesis. J. Neurosci. *29*, 11852–11858.

Kempermann, G., Song, H., and Gage, F.H. (2015). Neurogenesis in the adult hippocampus. Cold Spring Harb. Perspect. Biol. *7*, a018812.

Kopel, H., Meshulam, M., and Mizrahi, A. (2009). Three-dimensional distribution patterns of newborn neurons in the adult olfactory bulb. J. Neurosci. Methods *182*, 189–194.

Lemasson, M., Saghatelyan, A., Olivo-Marin, J.-C., and Lledo, P.-M. (2005). Neonatal and adult neurogenesis provide two distinct populations of newborn neurons to the mouse olfactory bulb. J. Neurosci. *25*, 6816–6825.

Lepousez, G., Valley, M.T., and Lledo, P.-M. (2013). The impact of adult neurogenesis on olfactory bulb circuits and computations. Annu. Rev. Physiol. *75*, 339–363.

Lepousez, G., Nissant, A., Bryant, A.K., Gheusi, G., Greer, C.A., and Lledo, P.-M. (2014). Olfactory learning promotes input-specific synaptic plasticity in adult-born neurons. Proc. Natl. Acad. Sci. USA *111*, 13984–13989.

Lin, C.-W., Sim, S., Ainsworth, A., Okada, M., Kelsch, W., and Lois, C. (2010). Genetically increased cell-intrinsic excitability enhances neuronal integration into adult brain circuits. Neuron *65*, 32–39.

Livneh, Y., and Mizrahi, A. (2011). Experience-dependent plasticity of mature adult-born neurons. Nat. Neurosci. *15*, 26–28.

Livneh, Y., Adam, Y., and Mizrahi, A. (2014). Odor processing by adult-born neurons. Neuron *81*, 1097–1110.

Lledo, P.-M., Alonso, M., and Grubb, M.S. (2006). Adult neurogenesis and functional plasticity in neuronal circuits. Nat. Rev. Neurosci. *7*, 179–193.

Lois, C., and Alvarez-Buylla, A. (1994). Long-distance neuronal migration in the adult mammalian brain. Science *264*, 1145–1148.

Magavi, S.S.P., Mitchell, B.D., Szentirmai, O., Carter, B.S., and Macklis, J.D. (2005). Adult-born and preexisting olfactory granule neurons undergo distinct experience-dependent modifications of their olfactory responses in vivo. J. Neurosci. *25*, 10729–10739.

Malvaut, S., and Saghatelyan, A. (2016). The role of adult-born neurons in the constantly changing olfactory bulb network. Neural Plast. *2016*, 1614329.

Mandairon, N., Sultan, S., Nouvian, M., Sacquet, J., and Didier, A. (2011). Involvement of newborn neurons in olfactory associative learning? The operant or non-operant component of the task makes all the difference. J. Neurosci. *31*, 12455–12460.

Miyamichi, K., Shlomai-Fuchs, Y., Shu, M., Weissbourd, B.C., Luo, L., and Mizrahi, A. (2013). Dissecting local circuits: parvalbumin interneurons underlie broad feedback control of olfactory bulb output. Neuron *80*, 1232–1245.

Mizrahi, A. (2007). Dendritic development and plasticity of adult-born neurons in the mouse olfactory bulb. Nat. Neurosci. *10*, 444–452.

Moreno, M.M., Linster, C., Escanilla, O., Sacquet, J., Didier, A., and Mandairon, N. (2009). Olfactory perceptual learning requires adult neurogenesis. Proc. Natl. Acad. Sci. USA *106*, 17980–17985.

Moreno, M.M., Bath, K., Kuczewski, N., Sacquet, J., Didier, A., and Mandairon, N. (2012). Action of the noradrenergic system on adult-born cells is required for olfactory learning in mice. J. Neurosci. *32*, 3748–3758.

Mouret, A., Lepousez, G., Gras, J., Gabellec, M.-M., and Lledo, P.-M. (2009). Turnover of newborn olfactory bulb neurons optimizes olfaction. J. Neurosci. *29*, 12302–12314.

Naritsuka, H., Sakai, K., Hashikawa, T., Mori, K., and Yamaguchi, M. (2009). Perisomatic-targeting granule cells in the mouse olfactory bulb. J. Comp. Neurol. *515*, 409–426.

Nissant, A., Bardy, C., Katagiri, H., Murray, K., and Lledo, P.-M. (2009). Adult neurogenesis promotes synaptic plasticity in the olfactory bulb. Nat. Neurosci. *12*, 728–730.

Orona, E., Scott, J.W., and Rainer, E.C. (1983). Different granule cell populations innervate superficial and deep regions of the external plexiform layer in rat olfactory bulb. J. Comp. Neurol. *217*, 227–237.

Otazu, G.H., Chae, H., Davis, M.B., and Albeanu, D.F. (2015). Cortical feedback decorrelates olfactory bulb output in awake mice. Neuron *86*, 1461–1477.

Pallotto, M., Nissant, A., Fritschy, J.-M., Rudolph, U., Sassoè-Pognetto, M., Panzanelli, P., and Lledo, P.-M. (2012). Early formation of GABAergic synapses governs the development of adult-born neurons in the olfactory bulb. J. Neurosci. *32*, 9103–9115.

Panzanelli, P., Bardy, C., Nissant, A., Pallotto, M., Sassoè-Pognetto, M., Lledo, P.-M., and Fritschy, J.-M. (2009). Early synapse formation in developing interneurons of the adult olfactory bulb. J. Neurosci. *29*, 15039–15052.

Petreanu, L., and Alvarez-Buylla, A. (2002). Maturation and death of adult-born olfactory bulb granule neurons: role of olfaction. J. Neurosci. *22*, 6106–6113.

Quast, K.B., Ung, K., Froudarakis, E., Huang, L., Herman, I., Addison, A.P., Ortiz-Guzman, J., Cordiner, K., Saggau, P., Tolias, A.S., and Arenkiel, B.R. (2017). Developmental broadening of inhibitory sensory maps. Nat. Neurosci. *20*, 189–199.

Ravi, N., Li, Z., Oettl, L., Bartsch, D., Schonig, K., and Kelsch, W. (2015). Postnatal subventricular zone progenitors switch their fate to generate neurons with distinct synaptic input patterns. Development *142*, 303–313.

Ravi, N., Sanchez-Guardado, L., Lois, C., and Kelsch, W. (2017). Determination of the connectivity of newborn neurons in mammalian olfactory circuits. Cell. Mol. Life Sci. *74*, 849–867.

Rochefort, C., Gheusi, G., Vincent, J.-D., and Lledo, P.-M. (2002). Enriched odor exposure increases the number of newborn neurons in the adult olfactory bulb and improves odor memory. J. Neurosci. *22*, 2679–2689.

Rokni, D., Hemmelder, V., Kapoor, V., and Murthy, V.N. (2014). An olfactory cocktail party: figure-ground segregation of odorants in rodents. Nat. Neurosci. *17*, 1225–1232.

Saghatelyan, A., Roux, P., Migliore, M., Rochefort, C., Desmaisons, D., Charneau, P., Shepherd, G.M., and Lledo, P.-M. (2005). Activity-dependent adjustments of the inhibitory network in the olfactory bulb following early postnatal deprivation. Neuron *46*, 103–116.

Sahay, A., Wilson, D.A., and Hen, R. (2011). Pattern separation: a common function for new neurons in hippocampus and olfactory bulb. Neuron *70*, 582–588.

Sailor, K.A., Valley, M.T., Wiechert, M.T., Riecke, H., Sun, G.J., Adams, W., Dennis, J.C., Sharafi, S., Ming, G.L., Song, H., and Lledo, P.M. (2016). Persistent structural plasticity optimizes sensory information processing in the olfactory bulb. Neuron *91*, 384–396.

Sakamoto, M., Imayoshi, I., Ohtsuka, T., Yamaguchi, M., Mori, K., and Kageyama, R. (2011). Continuous neurogenesis in the adult forebrain is required for innate olfactory responses. Proc. Natl. Acad. Sci. USA *108*, 8479–8484.

Sakamoto, M., Ieki, N., Miyoshi, G., Mochimaru, D., Miyachi, H., Imura, T., Yamaguchi, M., Fishell, G., Mori, K., Kageyama, R., and Imayoshi, I. (2014). Continuous postnatal neurogenesis contributes to formation of the olfactory bulb neural circuits and flexible olfactory associative learning. J. Neurosci. *34*, 5788–5799.

Tian, L., Hires, S.A., Mao, T., Huber, D., Chiappe, M.E., Chalasani, S.H., Petreanu, L., Akerboom, J., McKinney, S.A., Schreiter, E.R., et al. (2009). Imaging neural activity in worms, flies and mice with improved GCaMP calcium indicators. Nat. Methods *6*, 875–881.

Urban, N.N., and Arevian, A.C. (2009). Computing with dendrodendritic synapses in the olfactory bulb. Ann. N Y Acad. Sci. *1170*, 264–269.

Veyrac, A., Sacquet, J., Nguyen, V., Marien, M., Jourdan, F., and Didier, A. (2009). Novelty determines the effects of olfactory enrichment on memory and neurogenesis through noradrenergic mechanisms. Neuropsychopharmacology *34*, 786–795.

Whitman, M.C., and Greer, C.A. (2007). Synaptic integration of adult-generated olfactory bulb granule cells: basal axodendritic centrifugal input precedes apical dendrodendritic local circuits. J. Neurosci. *27*, 9951–9961.

Wienisch, M., and Murthy, V.N. (2016). Population imaging at subcellular resolution supports specific and local inhibition by granule cells in the olfactory bulb. Sci. Rep. *6*, 29308.

Wienisch, M., Blauvelt, D.G., Sato, T.F., and Murthy, V.N. (2012). Two-photon imaging of neural activity in awake, head-restrained mice. Neuromethods *67*, 45–60.

Willmore, B., and Tolhurst, D.J. (2001). Characterizing the sparseness of neural codes. Network *12*, 255–270.

Winner, B., Cooper-Kuhn, C.M., Aigner, R., Winkler, J., and Kuhn, H.G. (2002). Long-term survival and cell death of newly generated neurons in the adult rat olfactory bulb. Eur. J. Neurosci. *16*, 1681–1689.

Yamaguchi, M., and Mori, K. (2005). Critical period for sensory experience-dependent survival of newly generated granule cells in the adult mouse olfactory bulb. Proc. Natl. Acad. Sci. USA *102*, 9697–9702.

STAR★METHODS

KEY RESOURCES TABLE

REAGENT or RESOURCE	SOURCE	IDENTIFIER
Antibodies		
Polyclonal anti-GFP conjugated to Alexa 488	Invitrogen	Cat#A-21311, RRID: AB_221477
Polyclonal anti-Iba-1	Wako	Cat#019-19741, RRID: AB_839504
Polyclonal anti-GFAP	Dako	Cat#Z0334, RRID: AB_10013382
Bacterial and Virus Strains		
pLenti-hSynapsin - tTad	Hioki et al., 2009	Addgene ID 99862
pLenti-TRE-dTomato-t2A-GCaMP5	Hioki et al., 2009; this paper	N/A
pLenti-TRE-dTomato-t2A-GCaMP6s	Hioki et al., 2009; this paper	Addgene ID 99864
Chemicals, Peptides, and Recombinant Proteins		
Ethyl tiglate	Sigma-Aldrich	Cat#W246018
Ethyl valerate	Sigma-Aldrich	Cat#290866
Allyl butyrate	Penta	Cat#01-16900
2-methoxypyrazine	Sigma-Aldrich	Cat#W330205
Ethyl propionate	Sigma-Aldrich	Cat#112305
2-heptanone	Sigma-Aldrich	Cat#537683
Acetophenone	Sigma-Aldrich	Cat#A10701
Isoamylamine	Sigma-Aldrich	Cat#126810
Ethyl acrylate	Sigma-Aldrich	Cat#E970-6
Valeric acid	Sigma-Aldrich	Cat#240370
Pyrrolidine	Sigma-Aldrich	Cat#P73803
Piperidine	Sigma-Aldrich	Cat#411027
Allyl tiglate	Sigma-Aldrich	Cat#W204307
Valeraldehyde	Sigma-Aldrich	Cat#110132
Isoamyl acetate	Penta	Cat#09-11002
Heptanal	VWR	Cat#TCH0025
Isoeugenol	Sigma-Aldrich	Cat#W246808
1-Pentanol	Sigma-Aldrich	Cat#138975
p-anis aldehyde	Sigma-Aldrich	Cat#A88107
Experimental Models: Organisms/Strains		
Mouse: C57BL/6	Charles River	JAX: 000664
Mouse: C57BL/6J	The Jackson Laboratory	JAX: 000664, RRID: IMSR_JAX:000664
Software and Algorithms		
Labview	National Instruments	http://www.ni.com/en-us.html
MATLAB	MathWorks	https://www.mathworks.com
pClamp	Molecular Devices	https://www.moleculardevices.com
Fiji	SciJava	http://fiji.sc/
Moco	Dubbs et al., 2016	https://github.com/NTCColumbia/moco

CONTACT FOR REAGENT AND RESOURCE SHARING

Further information and requests for resources and reagents should be directed to and will be fulfilled by the Lead Contact, Venkatesh Murthy (vnmurthy@fas.harvard.edu).

EXPERIMENTAL MODEL AND SUBJECT DETAILS

Mice used in this study were adult, 8 to 12-week-old C57BL/6 males (Charles River and Jackson Laboratories) that were between 21 and 28 g at the beginning of the study. Mice were singly housed after chronic cranial window implantation. No randomization was used to assign animals to experimental groups (control versus enriched or imaging for young versus mature abGCs). All procedures were performed using approved protocols in accordance with institutional (Harvard University Institutional Animal Care and Use Committee) and national guidelines.

METHOD DETAILS

Surgery

Mice were anesthetized with an intraperitoneal injection of ketamine (100-150 mg/kg) and xylazine (10-15 mg/kg) and body temperature was maintained at 37°C by a heating pad. For viral injections, a small craniotomy was made bilaterally over the RMS injection sites (coordinates from bregma: A +3.3, L +0.82, from the brain surface: V −2.9 and −2.7) and 250 nL of lentivirus (1:1 mixture of both constructs, or in cases where sparser labeling was desired, between 1:10 to 1:50 dilution of the tTA-containing construct) was injected at each of the two depths using a pulled glass micropipette (tip diameter approximately 10-20 um). A chronic cranial window was implanted over both olfactory bulbs by making a craniotomy using a 3 mm biopsy punch as previously described. (Adam and Mizrahi, 2011). The cranial window surgery took place either 4-5 weeks before viral injection or 3-4 days after viral injection (see Figure S4). The surface was kept moist with artificial cerebrospinal fluid (125 mM NaCl, 5 mM KCl, 10 mM Glucose, 10 mM HEPES, 2 mM CaCl2 and 2mM MgSO4 [pH 7.4]) and Gelfoam (Patterson Veterinary) and a glass window consisting of two 3 mm No. 1 coverslips (Warner) glued together with optical glue (Norland Optical Adhesive 61) was implanted as previously described (Adam and Mizrahi, 2011). The edges were sealed with Vetbond (3M) and then C&B-Metabond dental cement (Parkell, Inc.). A custom-made titanium headplate was cemented to the skull. After surgery, mice were treated with carprofen (6 mg/kg) every 24 hours and buprenorphine (0.1 mg/kg) every 12 hours for 5 days. For imaging in resident GCs, the same procedures were followed, except that lentivirus was injected into the granule cell layer of the olfactory bulb (coordinates: A 1.0 relative to relative to intersection of inferior cerebral vein and superior sagittal sinus, L 0.6 relative to intersection of inferior cerebral vein and superior sagittal sinus, and V −0.6 to −1.1 from the brain surface) at P25-P31 and imaging was performed at P95-P100. For the subset of experiments involving doxycycline, mice were given access to chow containing doxycycline (200 mg/kg, Bio-Serv) *ad libitum* for 3 months, beginning on the day of viral injection in the bulb and ending 9 days before the start of imaging. All experiments were approved by the Standing Committee on the Use of Animals in Research of Harvard University.

Viral Vectors

We used a Tet-Off lentiviral system (Hioki et al., 2009) with one construct expressing the transactivator tTAad under control of a synapsin promotor and a second construct expressing dTomato-T2A-GCaMP5 or dTomato-T2A-GCaMP6s under control of a TRE promoter. VSV-G pseudotyped lentiviral vectors were produced by transfection of human embryonic kidney cells (HEK293FT) with third-generation lentivirus plasmids using lipofection (Mirus). Supernatant was collected 48 h after transfection and concentrated using centrifugal filters (Millipore). Plasmids used in this study are available at https://www.addgene.org/Venkatesh_Murthy/.

Immunohistochemistry

Mice were deeply anesthetized with a ketamine/xylazine mixture and perfused transcardially with 20 mL of PBS (pH 7.4) first, followed by 30-50 mL of 4% paraformaldehyde in 0.1 M phosphate buffered saline (pH 7.4). Brains were removed and cut into 70 um-thick sagittal sections for anti-GFP staining and 40 um thick sagittal sections for GFAP and IBA-1 staining with a vibratome (Leica). For anti-GFP staining, sections were permeabilized and blocked with a solution containing 0.1% Triton X-100 (Fisher), 0.5% carrageenan (Sigma), and 2.5% goat serum (Sigma) in PBS for 1 h, and incubated overnight with primary antibody against GFP conjugated to Alexa 488 dye (Invitrogen, A-21311, RRID:AB_221477) diluted 1:1000 in blocking solution. For GFAP and Iba-1 staining, slices were permeabilized and blocked with a solution containing 0.1% Triton X-100 (Fisher), and 5% goat serum in PBS for 1 hour at room temperature and then incubated overnight at 4°C with the primary antibodies rabbit anti-Iba-1 (Wako: 019-19741, RRID:AB_839504) at 1:500 or rabbit anti-GFAP (Dako: Z0334, RRID: AB_10013382) at 1:1000. They were then washed in PBS and incubated with secondary antibodies (Alexa goat-647 anti-Rabbit) for 2 hours at room temperature. Slices were then washed and mounted for confocal imaging with DAPI mounting media and imaged with a confocal microscope (LSM 710 or 880, Zeiss).

In Vivo Imaging

Animals were allowed to recover from surgery for at least three days prior to imaging. Animals were anesthetized with an intraperitoneal injection of ketamine and xylazine (90% of dose used for surgery) and body temperature was maintained at 37°C by a heating pad. A custom-built two-photon microscope (Wienisch et al., 2012) was used for *in vivo* imaging. Fluorophores were excited and imaged with a water immersion objective (20 × , 0.95 NA, Olympus) at 950 nm or 930 nm using a Ti:Sapphire laser (Mai Tai HP, Spectra-Physics). Frame rates were typically 4 Hz, the pixel size was 0.5 μm, and fields of view were typically 150 × 150 μm. The

point spread function of the microscope was measured to be 0.51 × 0.48 × 2.12 μm. Image acquisition and scanning were controlled by custom-written software in Labview. Emitted light was routed through two dichroic mirrors (680dcxr, Chroma and FF555- Di02, Semrock) and collected by two photomultiplier tubes (R3896, Hamamatsu) using filters in the 500-550 nm range (green channel, FF01-525/50, Semrock) and 572-642 nm range (red channel, FF01-607/70, Semrock).

To locate regions for imaging, a low magnification z stack (~300-500 μm square) at slow scanning speed (usually 0.5 Hz) with a 1-2 μm z step was taken from the surface of the dura to the granule cell layer (Movie S1). Planes with many dendrites perpendicular to the imaging axis were chosen for imaging during odor stimulation, and the three dimensional coordinates were recorded. With careful repositioning of the headplate in the imaging stage, a comparison with coordinates from previous imaging sessions, and observation of blood vessels on the brain surface, we were able to locate the general area that had been previously imaged. More exact repositioning could be accomplished using previously recorded low magnification z stacks. With the advantage of sparse labeling, we were able to relocate previously imaged neurons with a high degree of accuracy in subsequent imaging sessions.

Imaging in Awake Animals

Animals were water-restricted for 1-2 days before being handled and accustomed to head-fixation for 1-2 days with manual delivery of water rewards (30-45 minute sessions each). They were then acclimated to the sound of the scan mirrors and odor delivery (using three odors not in the imaging panel) for the day before imaging. All animals in the awake imaging experiment had never before experienced the imaging odors in an awake state, so the first trial was excluded due to possible changes in sniffing in response to novel odors (Kato et al., 2012). Immediately after imaging the animal in the awake state, ketamine/xylazine was injected subcutaneously (90% of dose used for surgery) and the same fields of view were imaged in the anesthetized animal. Odor set C was used for awake imaging, identical to odor set B but excluding isoamylamine and the mixture since these odors were found to be aversive to awake mice.

Odor Stimulation

Odor lists are found in Table S1. For odor set A, monomolecular odorants were used as stimuli and delivered by a custom-built 20 channel olfactometer controlled by custom-written software in Labview (National Instruments). Individual odors were presented for 5 s with an interstimulus interval of 60 s. Odorants were used at a nominal volumetric concentration of 1% (v/v) in mineral oil. Because limits on the length of repeated imaging sessions in anesthetized animals (imaging sessions were kept to 3-4 hours or less) necessitated a choice between stimulus panel size and the number of repetitions of each odor, for these experiments we delivered 1-2 repetitions of each odor.

Experiments with odor set B were performed with a different custom-built 16 channel olfactometer (Rokni et al., 2014). Odorants were used at a nominal volumetric concentration of 16% (v/v) in mineral oil and further diluted by 16 times in air. In this case, odors were presented for 2 s with an interstimulus interval of 40 s. Odors were delivered 3-5 times each. A photoionization detector (miniPID, Aurora Scientific) was used to measure odor concentrations to ensure that they remained consistent between trials.

Odor Enrichment

For the enrichment experiments, a large tea ball infuser (2 1/4 inch diameter) containing a Whatman filter paper circle was placed in the home cage. Every 24 hours beginning 5 to 7 days after viral injection in the RMS, a mixture containing half of the odors (50 μl at a nominal volumetric concentration of 10% (v/v) in mineral oil) from set A was placed on the filter paper, and the filter paper was replaced daily, alternating between odors 1-9 and odors 12-20.

Electrophysiology

Mice (8-12 weeks old at the time of lentivirus injection) were deeply anesthetized with a mixture of ketamine (100 mg/kg) and xylazine (10 mg/kg) and perfused with ice-cold modified ACSF solution (in mM: 120 choline chloride, 25 glucose, 25 NaHCO3, 2.5 KCl, 0.5 CaCl2, 7 MgSO4, 11.6 ascorbic acid, 3.1 pyruvic acid, 1.25 NaH2PO4). Brains were removed and placed in the same ice-cold modified ACSF. Horizontal slices (300 μm thick) of olfactory bulbs were cut using a vibratome (VT1000S; Leica, Germany). Slices were incubated in oxygenated holding solution (in mM: 119 NaCl, 26.2 NaHCO3, 1 NaH2PO4*H2O, 2.5 KCl, 22 glucose, 1.3 CaCl2, 2.5 MgSO4) at 32°C for at least 30 minutes before being transferred to oxygenated ACSF (in mM: 119 NaCl, 26.2 NaHCO3, 1 NaH2PO4*H2O, 2.5 KCl, 22 glucose, 2.5 CaCl2, 1.3 MgSO4). Whole-cell recordings (acquisition rate 10 kHz) were performed using patch pipettes filled with internal solution (in mM: 125 potassium gluconate, 10 HEPES, 1 EGTA, 2.0 Na2-ATP, 0.5 Na3-GTP, 0.025 CaCl2, 2 MgCl2, pH 7.3) using a Multiclamp 700B amplifier (Molecular Devices, Palo Alto, CA) at 35°C. Cells were visualized with dTomato and DIC with custom-built optics on a BX51WI microscope (Olympus Optical, Tokyo, Japan) and recorded with pClamp 10.3 (Molecular Devices). Cell identity was confirmed by the presence of fluorescence material in the patch pipet after membrane rupture and/or cell fill with Alexa Fluor 488, and only cells that had a proximal dendrite that extended at least 50 μm from the soma in the direction of the EPL were included in the dataset.

Cells with a series resistance of < 60 MΩ and holding current (at −70 mV) of < 100 pA were used for analysis. Analysis of current-clamp data was performed using custom-written scripts in MATLAB. All spikes with amplitude greater than 10 mV were detected. Current steps (1 s) were applied in increments of 1 pA at a holding voltage of approximately −65 mV. If the holding voltage deviated

from −65 mV by more than 10 mV for any single step, that step was excluded, and cells with 5 consecutive trials that deviated from the target holding voltage were excluded. Cells that never fired an action potential (1/11 dTomato cells and 4/21 dTomato-GCaMP6s cells) were excluded from threshold current, amplitude, and half-width analyses. Threshold current was defined as the first of two consecutive current steps that evoked at least one action potential. Single action potential parameters (peak amplitude and half-width) were measured at threshold.

QUANTIFICATION AND STATISTICAL ANALYSIS

In Vivo Imaging Analysis

Data were analyzed offline using custom-written scripts in MATLAB (Mathworks). Experimenters were blind to fluorescence changes during data analysis but not to the age of the cells or experimental group.

Regions of Interest

We selected regions of interest (ROIs) representing dendritic segments for analysis from average intensity projections in the dTomato channel. All dendrites meeting the following criteria were selected for analysis for population data (Figures 2 and 6): (i) Dendrite was clearly distinguishable from the occasional labeled axons based on width and presence of spines (ii) Dendrite did not belong to a PG cell as shown by z stacks (iii) Dendrite had typical morphology of a granule cell dendrite – it branched in the EPL, and converged with other dendrites into a single apical dendrite with increasing imaging depth. A z stack was taken for each imaging region, from the surface of the dura down to the convergence of GC dendrites into a single apical dendrite. In general, for FOVs imaged early on (6-10 dpi), it was possible to assign each dendrite to its parent cell based on z stacks. For data involving cells tracked over weeks (Figures 3, 4, and 5), we used the z stack taken on the first day to determine which ROIs belonged to the same cell, and data from these ROIs were averaged if all ROIs from the same cell were accurately tracked across all days, or the ROI that was tracked in the greatest number of imaging sessions was chosen to represent that cell. For population data (Figures 2 and 6), it was impossible to accurately assign ROIs to a parent cell at the later imaging times (35-45 dpi) because the labeling became more dense over time as dendrites grew and newcomers arrived. Therefore, some dendrites in these datasets belong to the same cell. Based on tracing dendrites to parent cells in the first week of imaging in the followed cells data, we found that the correction factor (number of ROIs divided by number of cells) ranged from 1 to 2.2 across all FOVs with an overall correction factor of 1.4; therefore, we estimate that there are 1.4 times more dendrites than cells represented in our population data. Fields of view were non-overlapping and separated by at least 50 μm edge to edge to minimize the chance of dendrites from the same cell appearing in multiple fields of view.

Motion Correction

To correct for fast lateral motion and image drift, all image frames for a given field of view were aligned to the average of the first trial using a frame-by-frame rigid transformation with a regular step gradient descent (for imaging in anesthetized animals) or cross-correlation based on rigid body translation for imaging in awake animals (ImageJ plugin Moco) (Dubbs et al., 2016). Frames with out of frame motion were removed based on the calculated cosine similarity between each frame and the average intensity projection of the first trial (or in the case of awake imaging, the first no odor trial, which tended to have the least motion). Image frames with cosine similarity that differed by more than 30% from the mean value for the user-determined best trial for that field of view or more than 20% from the mean of the baseline period for that particular trial were discarded. In some trials, immersion water dried up or laser power fluctuated, so trials were removed if their average brightness was less than half of the brightness of the average of the first three trials or if difference in brightness between the baseline and odor periods was greater than three times the standard deviation of brightness in the first trial. The entire trial was removed if, after these corrections, it contained less than 75% of the original frames.

Tracking ROIs

For data on sequentially tracked cells (Figures 3, 4, 5, and 7), ROIs were chosen to include dendrites but not spines in order to minimize the effects of changes in spines on the analysis. Whenever possible, images were aligned across days using an affine transformation with a regular step gradient descent (MATLAB function imregister) and the ROI mask from the first day was applied to all subsequent days. When automatic registration failed (in cases where there were significant changes in dendritic morphology or many new dendrites), matching ROIs were chosen manually. In all cases, followed ROIs were manually reviewed for every day of imaging. ROIs that were out of focus or obscured by a new dendrite were discarded for that day of imaging.

Newcomers

Cells were classified as ''newcomers'' if a new dendrite (not visible in the average intensity projection from the previous week, even after adjusting the brightness and contrast in ImageJ) appeared in a FOV and if image stacks confirmed that a new apical dendrite (or cell body, if it was sufficiently superficial) had appeared, to which the new dendrite belonged.

Fluorescence Changes

The average intensity in the green (GCaMP) channel was calculated for each ROI, for each frame and for each odor. A response value for each cell-odor pair was calculated as the average ΔF/F value over the 5 s of odor presentation where F represents the average baseline fluorescence in the ROI. For most of our data we found that baseline GCaMP fluorescence was so low in abGC dendrites that we could not reliably subtract the background. Therefore, for Figures 3, 4, 5, 7, S2, S3A–S3D, S6, and S7, we report raw ΔF/F. For

all other figures, we report $\Delta F/F_\sigma$ where F_σ is the standard deviation of fluorescence during the baseline period. We confirmed that the choice of measure did not affect our conclusions (Figure S5D). For all data, fluorescence change values were calculated for each available repeat of an odor stimulus (after bad frames or trials were removed as described above), and the mean was taken across all repetitions. Bleaching was corrected by fitting a single exponential to the florescence during the baseline period and taking the value at the end of the baseline period as the baseline mean, only for ROIs where the fluorescence during the last 2.5 s of the baseline period was greater than 1.1 times the fluorescence during the first 2.5 s. If, after correction for bleaching, baseline F_σ was greater than 30% (for population data) or 40% (for tracked cells data) of the mean baseline fluorescence, that ROI was considered too noisy and was removed from the analysis.

Thresholds

For all figures where a threshold was applied to the data, thresholds were calculated based on the distribution of "no odor" trials. An area under the receiver operating curve analysis was performed and the lowest threshold yielding 10 responses for every 1 no odor response was chosen. For data obtained with GCaMP5/odor set A, "no odor" trials were not included. Therefore, a mock noise distribution was created by combining the raw fluorescence values for the baseline periods for all the trials for a given ROI and then sampling from these values to calculate a mock "no odor" $\Delta F/F$ value for each ROI. The same ROC analysis as described above was then used on this distribution. Thresholds were calculated for each figure by combining responses from all experimental groups (i.e., young and mature or awake and anesthetized) and performing ROC analysis on the combined data.

Lifetime Sparseness

We applied the threshold to the data and then used the following equation to calculate lifetime sparseness (Wienisch and Murthy, 2016; Willmore and Tolhurst, 2001):

$$LS = \frac{\left(\sum_{j=1}^{m} \frac{r_j}{m}\right)^2}{\left(\sum_{j=1}^{m} \frac{r_j^2}{m}\right)}$$

where m = number of odors, r_j = response of the neuron to odor j.

If all stimuli activate a cell rather uniformly, LS will be close to 1, and if only a small fraction of the stimuli activate a cell significantly, LS will be close to 0. For any cells with all responses below threshold, we set LS = 0, interpreting this as the sparsest possible representation.

Temporal Dynamics

Principal component analysis of the time course of responses was performed in MATLAB using centered data and singular value decomposition as described previously (Wienisch and Murthy, 2016). To compare time courses for young and mature cells, principal components were calculated on each dataset (all traces from all cell-odor pairs) separately and the angle between the two spaces spanned by the coefficient vectors for the first three principal components was calculated. Then the group to which each trace belonged was shuffled 1,000 times, and the angles between new coefficient vectors were calculated based on random division into two groups of the same size as the original datasets. The actual angle was then compared to this distribution to obtain a p value.

Ranked Odor Curves

As described previously (Wienisch and Murthy, 2016), to facilitate averaging of odor tuning curves across all cells, we ordered individual tuning curves in descending order of amplitudes and averaged them across all cells. We compared these curves between groups or to a noise distribution obtained by performing the same analysis on resampled no odor responses to determine the average number of odors to which a cell responds.

Response Categories

Dendrite-odor pairs that were not measured on one of the paired weeks were discarded. A threshold was applied to the responses, and dendrite-odor pairs were divided into one of four categories based on whether a response was above threshold on both weeks ("stable"), one week ("disappeared" or "new"), or neither of the weeks ("no response") (Figures 4B, 7G, and 7H).

Tuning Similarity

If the response of a dendrite was not measured for any odor on one of the paired weeks, it was discarded from the analysis. The tuning curves of all qualifying dendrites were thresholded and one minus the Hamming distance was calculated according to the following equation:

$$\text{Tuning similarity} = 1 - \text{HD where } HD = \left(\frac{\#(x_i \neq y_i)}{m}\right)$$

where m = number of odors

x_i and y_i are strings of zeros and ones representing whether a response was greater than the threshold.

Bootstrapping

Bootstrapped confidence intervals were calculated from 1,000 samples using the bias-corrected and accelerated percentile method.

Testing Independence of Dendrite-Odor Pairs

For analyses in Figures S6D and S6E, to test whether dendrite-odor pairs behaved independently (between a given pair of weeks), we calculated the conditional probability that a response would appear or disappear based on its presence in the previous week (based on the behavior of all dendrite-odor pairs between those two weeks, see Response categories). We then constructed predicted tuning curves for all dendrites on the second week to obtain a predicted number of responses lost or gained (mean of predicted number of responses lost or gained across 1,000 repeats) and calculated the following indices:

$$\text{Gain index} = \frac{\text{actual number gained} - \text{predicted number gained}}{m}$$

$$\text{Loss index} = \frac{\text{actual number lost} - \text{predicted number lost}}{m}$$

where m = total number of odors.

Normalized Odor Tuning

Normalized odor tuning was calculated as the number of responses above threshold divided by the total number of odors (Figures 3, 4, 5, and 7). Normalized odor tuning was considered significantly different from weeks 1-2 to weeks 6-7 if it fell outside the 95% confidence interval of tuning curves based on simulating the initial tuning curve 1,000 times with the average CV of the population, 41.4%.

Cosine Similarity over Time

We calculated the cosine of the angle between vectors of pixels in each ROI on each pair of weeks (Figure S6B). If the ROIs were different sizes on different weeks (as happened when automatic registration failed and corresponding ROIs were drawn manually), then the smaller ROI was centered on the larger ROI and the extra pixels from the larger ROI were removed before calculating the cosine similarity.

Cranial Window Inflammation Analysis

Images were taken with a confocal microscope (Zeiss LSM 880). Laser power and gain were optimized for the dimmest sample and applied to all other slices. Five μm z stacks consisting of 16 bit images (1024x1024 pixels) were compressed to maximum intensity projections. Regions of interest in the EPL and GCL were drawn and the areas were measured with ImageJ. The Cell Counter plugin (Fiji) was used to count all GFAP and Iba-1 positive cell bodies within these areas of interest, and the density of cells per 100 μm^2 was calculated for each image. Mean fluorescence intensity within these areas was also calculated. These measures were calculated for two large fields of view (600x600 um) on the dorsal surface of each bulb taken from two different slices and averaged to obtain one measure per bulb.

Statistical Tests

Non-parametric statistical tests were used for most comparisons, so no assumption of normality of data was made. Details for each statistical test can be found in the corresponding figure legend, and the rationale behind each is described here. The Wilcoxon signed rank test was used to compare repeated-measurements on the same cells. The two-sided Wilcoxon rank sum test was used for comparing all unpaired non-normal distributions. The Kolmogorov-Smirnov test was used to compare cumulative probability distributions. The Cochran–Mantel–Haenszel test was used to compare matched categorical data. The Bonferroni multiple comparisons correction was applied for all comparisons involving multiple measurements per dendrite or cell, and this is stated in the text and figure legend (uncorrected p values are reported, along with the corrected significance threshold which is calculated by dividing the significance level by the number of repeated-measurements, i.e., the number of odors), and stars refer to the corrected threshold. A chi square goodness of fit test was used to compare distributions of the proportion of dendrites falling into response categories. For all experiments, between 4 and 7 animals per experiment were used, with the number per group stated in each legend. Effort was made to minimize the number of animals used and to obtain the maximum amount of data per animal. Animals that did not have labeled cells in a clear area of the cranial window were excluded (approximately 30%–40% of animals that underwent cranial window surgery and/or viral injection with the intention of imaging abGCs were excluded for this reason). Data from two fields of view for mature somata (Figure S3) were excluded because the animal's breathing rate was slower than 1 Hz due to problems with anesthesia. Two animals were excluded from the young dendrites population data (Figure 2) because measured odor concentrations with a PID were not consistent with concentrations during the rest of the experiment. The number of animals used and the number of trials or repetitions per animal were large enough to obtain a dataset with statistical power and are congruent with previously published studies in the field (for example, Livneh et al., 2014; Sailor et al., 2016). Variance within a group was described as SEM or as interquartile range where noted in the figure legend. All n values for each statistical test can be found at the end of each figure legend and are also stated here. For abGC population data in Figure 2, n = 256 young and 405 mature dendrites in 7 mice (4 of which were the same for each group and 3 of which were different), respectively, with 48, 32, 9, 102, 34, 12, and 19 young dendrites from each mouse and 63, 37, 93, 60, 44, 49, and 59 mature dendrites from each mouse. For the tracked abGCs in Figures 3, 4, and 5, n = 149 dendrites, each traced to a unique cell, in 6 mice. Of these, 41 dendrites were imaged with GCaMP5 and odor set A for at least two weeks, with 33 of them imaged for at least 6 weeks. 108 dendrites were imaged with GCaMP6s and odor set B, and 68 of these dendrites were

imaged for at least 5 weeks. For imaging in awake mice, n = 152 young and 228 mature dendrites from 4 mice per group. For the tracked abGCs in enriched mice in Figure 7, n = 7, 51, 44, 42, 40, 18, and 15 dendrites for each week of imaging from 3 enriched mice. For analyses on dendrite-odor pairs, the number of dendrite-odor pairs is equal to the number of dendrites (above) times the number of odors (20 odors in set A, 9 odors in set B, and 7 odors in set C). In these cases, the Bonferroni correction for multiple comparisons was applied to correct for the number of repeated-measures (i.e., the number of odors) made on each dendrite or cell.

DATA AND SOFTWARE AVAILABILITY

All data are available from the Lead Contact, Venkatesh N. Murthy (vnmurthy@fas.harvard.edu), upon request.